

*AB INITIO* CALCULATIONS OF INTRAMOLECULAR EXCITON TRANSFER WITH  
REDUCED MODES IN DONOR-BRIDGE-ACCEPTOR SPECIES

---

A Dissertation Presented to  
the Faculty of the Department of Chemistry  
University of Houston

---

In Partial Fulfillment  
of the Requirements for the Degree  
Doctor of Philosophy

---

By  
Xunmo Yang  
May 2016

*AB INITIO CALCULATIONS OF INTRAMOLECULAR EXCITON TRANSFER WITH  
REDUCED MODES IN DONOR-BRIDGE-ACCEPTOR SPECIES*

---

Xunmo Yang

APPROVED:

---

Dr. Eric R. Bittner, Chairman

---

Dr. Vassiliy Lubchenko

---

Dr. Shoujun Xu

---

Dr. Don Coltart

---

Dr. Gila Stein  
Department of Chemical and Biomolecular Engineering

---

Dean, College of Natural Sciences and Mathematics

---

Out yonder there was this huge world, which exists independently of us human beings and which stands before us like a great, eternal riddle, at least partially accessible to our inspection and thinking. The contemplation of this world beckoned as a liberation, and I soon noticed that many a man whom I had learned to esteem and to admire had found inner freedom and security in its pursuit. The mental grasp of this extra-personal world within the frame of our capabilities presented itself to my mind, half consciously, half unconsciously, as a supreme goal. Similarly motivated men of the present and of the past, as well as the insights they had achieved, were the friends who could not be lost.

- Albert Einstein

## ACKNOWLEDGMENTS

---

I would like to express my sincere gratitude to Vas Lubchenko, whose support often extended well beyond of what is normally required from the graduate advisor. I am also thankful to him for very careful, critical, and multiple reading of this manuscript which greatly contributed to its quality. This work would not be possible without help of my family: my parents, my wife, and my son. I am deeply grateful to Eric R. Bittner who, by being such a wonderful graduate advisor to my wife, made an inconspicuous, but very important, influence on everything I did. I also would like to thank to Anne Goj, Jon Golden, Pyotr Rabochiy, and other members of Bittner and Lubchenko's groups who made this place such a nice professional home. I am indebted to Elena and Phil Motuzko for helping me in the time of need. Last but not least, I thank Sergei Lukyanets without whom I would never became a scientist.

The numerical part of this work was completed using TLC2 HPC facility of the University of Houston and Ares cluster of the Texas Southern University. I am especially indebted to C. J. Tymczak for providing the access to the latter.

I also gratefully acknowledge support by the Donors of the ACS Petroleum Research Fund, the Arnold and Mabel Beckman Foundation, the Welch Foundation Grant E-1765, and the NSF Grant CHE 0956127.

*AB INITIO* CALCULATIONS OF INTRAMOLECULAR EXCITON TRANSFER WITH  
REDUCED MODES IN DONOR-BRIDGE-ACCEPTOR SPECIES

---

An Abstract of a Dissertation Presented to  
the Faculty of the Department of Chemistry  
University of Houston

---

In Partial Fulfillment  
of the Requirements for the Degree  
Doctor of Philosophy

---

By  
Xunmo Yang  
May 2016

## ABSTRACT

---

Essential microscopic aspects of activated transport in liquids, which precedes the glass transition, have evaded explanation for decades. These poorly understood aspects include: the molecular underpinning of the excess, configurational entropy; the transition state configurations for the activated transport; the chemical origin of the fragile vs. strong liquid behavior; and many others. This dissertation puts forth a radically novel way to address these open questions, in which liquids near their glass transition are viewed as structurally degenerate assemblies of strongly interacting, local sources of frozen-in stress. The thermodynamics and activated barriers for rearrangement of this stress field have been mapped onto a Heisenberg model with six-dimensional spins. A meanfield analysis of the spin model has shown glasses can be viewed as frozen-in patterns of shear stress and/or uniform compression/dilation, the two extremes corresponding to the strong and fragile behaviors. A self-consistent elasticity theory of aperiodic, metastable solids emerges in the present analysis; it supersedes the traditional elasticity theory, which fails to self-consistently account for the structural degeneracy stemming from the inherent mismatch between cohesive forces and steric repulsion. The observable elastic constants self-consistently emerge in the present theory similarly to how the dielectric susceptibility is determined by the properties of molecular dipoles. First simulations of the spin model have been carried out. In addition to direct observations of transition states for the activated transport, several key features of the glass transition are yielded by the spin model, including a strongly non-exponential, non-Arrhenius character of the relaxations and its correlation with the Poisson ratio of the substance.

## CONTENTS

---

1	CHAPTER 2	1
1.1	INTRODUCTION	1
1.2	THEORETICAL APPROACH	4
1.2.1	<i>Model Hamiltonian</i>	4
1.2.2	<i>Non-Markovian Master Equation and Golden-Rule rates</i>	6
1.2.3	<i>Parameterization From Quantum Chemistry</i>	7
1.3	ENERGY TRANSFER RATES IN DONOR-BRIDGE-ACCEPTOR SYSTEMS	10
1.4	DETERMINING THE OPTIMAL ELECTRON-PHONON COUPLING COMPONENTS	12
1.4.1	<i>Lanczos Method</i>	14
1.5	DISCUSSION	21
2	CHAPTER 3	26
2.1	INTRODUCTION	26
2.2	THEORETICAL MODEL	28
2.2.1	<i>Hamiltonian and Parameterization</i>	28
2.2.2	<i>Transition Rate and Autocorrelation</i>	31
2.2.3	<i>Constructing Primary Lanczos Modes</i>	32
2.3	SYMMETRY OF THE PRIMARY LANCZOS MODES	35
2.4	LOCALIZED PROPERTY OF THE PRIMARY LANCZOS MODE	38
2.5	GEOMETRY CHANGE AND RELAXATION MODE	43
2.6	DISCUSSION	47

## LIST OF FIGURES

---

- Figure 1 Sketch of Marcus parabolas for a model energy or charge transfer system. Labeled are the key parameters used to compute the Marcus rate constant (Eq. 1). Energies are given in eV and the collective nuclear displacement is dimensionless. 2
- Figure 2 Adiabatic energy curves and off-diagonal couplings computed along an interpolation coordinate between the  $D^* - B - A$  and  $D - B - A^*$  equilibrium geometries.  $V_{ab}$  is the off-diagonal coupling at each point along this coordinate. 9
- Figure 3 Comparison between predicted (TCLME) rate constants and the experimental rates from Ref.[5]. With exception of the methyl and D-2,6-ea bridged cases, the TCLME results are in good agreement with the experimental results. 12
- Figure 4 Primary coupling modes for (a) c-1,4ee and (b) d-2,6ae projected onto the atomic displacement coordinates. 17
- Figure 5 Convergence of the electronic coupling autocorrelation function (Eq. 1.27) with respect to number of reduced modes. 19
- Figure 6 Comparison between exact rate constant and its primary mode approximation. The blue points correspond to rates computed using only the primary mode and the reorganization energy for only that mode. The red points use the primary mode and the exact renormalized energies. 20
- Figure 7 Molecular structure of naphthalene donor and a benzaldehyde acceptor linked by various bridging units. 28
- Figure 8 Primary Lanczos modes for (a) c14ee and (b) d26ae projected onto the atomic displacement coordinates. The frequencies for both these are at 0.185 eV ( $1490 \text{ cm}^{-1}$ ), a typical  $C = C$  stretching frequency for arene systems. 34
- Figure 9 Projection of PLMs onto (a) benzaldehyde in c14ee (b) symmetrized naphthalene in c14ee, (c) benzaldehyde in d26ae and (d) symmetrized naphthalene in d26ae. The normal modes are listed from low to high frequency and the irreducible representations of the dominant modes are color-coded. The assigned IRs for naphthalene are exact whereas the IRs are only approximate for benzaldehyde. 36
- Figure 10 The correlation functions of projected modes for c14ee with the naphthalene moiety replaced by (a) phenyl ring and (b) anthracene, with their PLMs shown in (c) and (d). 37
- Figure 11 The (a) ( $A_u$ ) HOMO and (b) ( $B_{2g}$ )LUMO of naphthalene. 38

Figure 12	Projections of the PLM onto the normal modes of (a) c14ee and (b) d26ae. 39
Figure 13	Projection of PLMs onto unsymmetrized naphthalene for (a) c14ee and (b) d26ae. They are almost same to Fig. 9(b) and (d) except for a mode with $B_{2u}$ symmetry in c14ee. Embedded are the most significant modes, namely, the 33rd modes 41
Figure 14	Correlation functions for different combinations of normal modes are shown for (a) c14ee and (b) d26ae. The “exact” ones refer are for the PLMs. “NfBf” is the mode made up from all normal modes of both the donor and acceptor sites. The designation “NxBy” indicates that the correlation function was constructed using $x$ most significant normal modes on naphthalene and $y$ most significant ones on benzaldehyde. Plots (c) and (d) show the relative error in rate constants calculated for various combinations of normal modes compared to the exact result or c14ee (c) and d26ae (d) respectively. 43
Figure 15	Projections of the geometry change between initial and final states onto the normal modes of (a) benzaldehyde and (b) naphthalene sites in c14ee, and d26ae in (c) and (d). Except for some low frequency modes, they are similar to the projections of PLM. 45
Figure 16	Projections of the geometry change between initial and final states onto the normal modes of (a) c14ee and (b) d26ae. They are both dominated by single mode, the relaxation mode (RM), which is embedded. 46
Figure 17	Correlation functions of relaxation mode (RM), PLM, geometry change (GC), and geometry change with the RM component eliminated for (a) c14ee and (b) d26ae. The exact rate is computed using the full set of normal modes. 48
Figure 18	Relative comparison of the rate constants computed using different sets of reduced modes. blue = c14ee, gold =d26ae. 49

## INDEX OF FREQUENTLY USED SYMBOLS

---

$\mathbf{r}, x_i$	Position vector
$\mathbf{u}, u_i$	Deformation field
$\boldsymbol{\varepsilon}, \varepsilon_{ij}, \varepsilon_\alpha$	Strain tensor (compatible)
$\boldsymbol{\sigma}, \sigma_{ij}, \sigma_\alpha$	Stress tensor (compatible)
$\rho, \rho_{ij}, \rho_\alpha$	Frozen-in stress field of amorphous structure (incompatible)
$\eta, \eta_{ij}, \eta_\alpha$	Strain corresponding to $\rho$ (incompatible)
$\epsilon^*, \epsilon_{ij}^*, \epsilon_\alpha^*$	Eigenstrain corresponding to $\rho$
$\mathbf{f}, f_i$	Body force field
$C, C_{ijkl}, C_{\alpha\beta}$	Elastic moduli tensor
$\lambda, \mu$	Lamé coefficients
$\kappa$	Bulk modulus
$\nu$	Poisson ratio
$g$	Order parameter of the crystal-to-glass transition
$a$	Size of the effective particle, or bead, in a glass
$s_c$	Configurational entropy per bead
$\epsilon_{ijk}$	Levi-Civita symbol
$c$	Number density
$\rho_M$	Mass density
$c_t$	Transverse sound velocity
$c_l$	Longitudinal sound velocity
$V$	Volume of a macroscopic body $\mathcal{B}$
$v$	Volume of a mesoscopic inclusion $\mathcal{I}$
$\beta$	Inverse temperature, $\beta = (k_B T)^{-1}$
$\theta$	Dimensionless inverse temperature, $\theta = \beta g^2 a^3$

## ACRONYMS

---

# 1

## CHAPTER 2

---

### 1.1 INTRODUCTION

Energy and electronic transport plays a central role in a wide range of chemical and biological systems. It is the fundamental mechanism for transporting the energy of a absorbed photon to a reaction center in light harvesting systems and for initiating a wide range of photo-induced chemical processes, including vision, DNA mutation, and pigmentation. The seminal model for calculating electron transfer rates was developed by Marcus in the 1950's[1–3].

$$k_{Marcus} = \frac{2\pi}{\hbar} |V_{ab}|^2 \frac{1}{\sqrt{4\pi k_B T \lambda}} e^{-(\lambda + \Delta\epsilon)^2 / 4\lambda k_B T}. \quad (1.1)$$

where  $\lambda$  is energy required to reorganize the environment following the transfer of an electron from donor to acceptor. and  $\Delta\epsilon$  is the driving force for the reaction.

If we assume that the nuclear motions about the equilibrium configurations of the donor and acceptor species is harmonic, the chemical reactions resulting from energy or charge transfer events can be understood in terms of intersecting diabatic potentials as sketched in Fig. 1. The upper and lower curves are the adiabatic potential energy surfaces describing the nuclear dynamics resulting from an energy or charge transfer event, taking the geometry of the donor state as the origin. As

---

o Part of this chapter has been published in Xunmo Yang and E. R. Bittner, The Journal of Physical Chemistry A **118**, 5196 (2014)

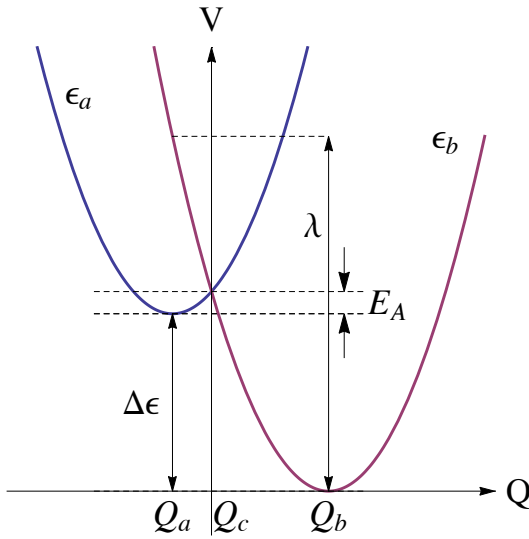


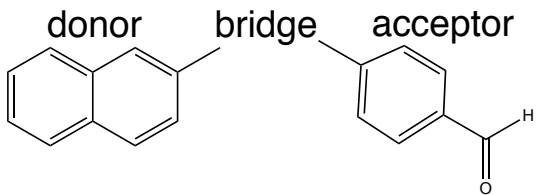
Figure 1: Sketch of Marcus parabolas for a model energy or charge transfer system. Labeled are the key parameters used to compute the Marcus rate constant (Eq. 1). Energies are given in eV and the collective nuclear displacement is dimensionless.

the transfer occurs by crossing an energy barrier, the transfer rate can be expected to be in the Arrhenius form

$$k \propto e^{-E_A/k_B T}, \quad (1.2)$$

with  $E_A$  as the activation energy. Using  $E_A = (\lambda + \Delta\epsilon)^2/4\lambda$  we can relate the activation energy to both the reorganization energy and driving force,  $-\Delta\epsilon$ . One of the most profound predictions of the theory is that as the driving force increases, the transfer rate reaches a maximum and further increases in the driving force lead to lower reaction rates, termed the inverted regime.

We focus here on the rates of triplet exchange between a naphthalene donor and a benzaldehyde acceptor linked by a variety of bridging units.



Triplet energy exchange in these systems occurs via the through-space Dexter mechanism[4]. This is a short-ranged interaction involving the simultaneous exchange of two electrons between the donor and acceptor moieties. Systems such as these formed the basis of a series of experiments by Closs and Miller[5] in which they verified the existence of the Marcus inverted regime and serve as crucial benchmarks for testing new theoretical models for computing energy and charge transfer rates[6–8].

A number of years ago, we developed a time-convolutionless master equation approach for computing state-to-state rates in which the coupling between states depends upon the nuclear coordinates[9]. This approach incorporates a fully quantum mechanical treatment of both the nuclear and electronic degrees of freedom and recovers well-known Marcus expression in the semiclassical limit. The model is parameterized by the vibrational normal mode frequencies, and the electronic energies and energy derivatives at a reference configuration. The approach has been used by our group to compute state-to-state transition rates in semi-empirical models for organic semiconducting light-emitting diode and photovoltaics [10–13]. This paper represents the first time we have used this approach within the context of a fully *ab initio* quantum chemical model. As such, this present work provides an important benchmark of the approach since all parameters will be determined using state-of-the-art quantum chemical methods and results compared to both theoretical and experimental rates.

Central to the work presented here is the use of a diabatization scheme for determining donor and acceptor states in a molecular unit. We benchmark the approach by computing the triplet energy transfer rates for a series of donor-bridge-acceptor molecules originally studied by Closs[5].

## 1.2 THEORETICAL APPROACH

The triplet energy transfer rates computed using our approach compare well against both the experimental rates and with more recent theoretical rates presented by Subotnik *et al.* [6–8]. An important component of our analysis is the use of a projection operator scheme that parses out specific internal nuclear motions that accompany the electronic transition. Similar decomposition schemes have been presented by Burghardt [14–17] and the approach used here builds upon the method given in Ref. [18]. By analyzing the electron-phonon couplings, we can discern a reduced set of motions that are responsible for coupling between the donor and acceptor states.

### 1.2 THEORETICAL APPROACH

#### 1.2.1 *Model Hamiltonian*

We consider a generic model for  $n$  electronic states coupled linearly to a phonon bath. Taking the electronic ground state of the system as a reference and assuming that the electronic states are coupled linearly to a common set of modes, we arrive at a generic form for the Hamiltonian:

$$H = \begin{pmatrix} \epsilon_1 & 0 \\ 0 & \epsilon_2 \end{pmatrix} + \begin{pmatrix} g_{11} & g_{12} \\ g_{21} & g_{22} \end{pmatrix} \cdot \mathbf{q} + \frac{\mathbf{p}^2}{2} + \frac{1}{2} \mathbf{q}^T \cdot \Omega \cdot \mathbf{q}. \quad (1.3)$$

Here, the first term contains the electronic energies,  $\epsilon_1$  and  $\epsilon_2$  computed at a reference geometry—typically that of the donor or acceptor state. The second term represents the linearized coupling between the electronic and nuclear degrees of freedom given in terms of the mass-weighted normal coordinates  $\mathbf{q}$ . The diagonal terms give the adiabatic displacement forces between the reference geometry and the two states. If we choose one of the states as the reference state, then either  $g_{11}$  or  $g_{22}$  will vanish. The remaining two terms correspond to the harmonic motions of the nuclear

## 1.2 THEORETICAL APPROACH

normal modes, given here in mass-weighted normal coordinates. In the normal mode basis,  $\Omega$  is diagonal with elements corresponding to the normal mode frequencies,  $\omega_j^2$ .

We now separate Eq. 2.7 into diagonal and off-diagonal terms

$$\hat{H} = \hat{H}_o + \hat{V} \quad (1.4)$$

and perform a polaron transform using the unitary transformation [9, 21, 22].

$$\begin{aligned} U &= e^{-\sum_{ni} \frac{g_{nni}}{\hbar\omega_i} |n\rangle\langle n| (a_i^\dagger - a_i)} \\ &= \sum_n |n\rangle\langle n| e^{-\sum_i \frac{g_{nni}}{\hbar\omega_i} (a_i^\dagger - a_i)} \end{aligned} \quad (1.5)$$

under which the transformed Hamiltonian is written in terms of the diagonal elements

$$\tilde{H}_0 = U^{-1} H_0 U = \sum_n \tilde{\epsilon}_n |n\rangle\langle n| + \sum_i \omega_i a_i^\dagger a_i, \quad (1.6)$$

with the renormalized electronic energies,

$$\tilde{\epsilon}_n = \epsilon_n - \sum_i \frac{g_{nni}^2}{\hbar\omega_i}, \quad (1.7)$$

and off-diagonal terms,

$$\hat{V}_{nm} = \sum_i g_{nni} \left( a_i^\dagger + a_i - \frac{2g_{nni}}{\hbar\omega_i} \right) e^{\sum_j \frac{(g_{nnj} - g_{mmj})}{\hbar\omega_j} (a_j^\dagger - a_j)}. \quad (1.8)$$

In the transformed (or dressed) picture the electronic transition from state  $|n\rangle$  to  $|m\rangle$  is accompanied by the excitations of all the normal phonon modes. Transforming to the interaction representation

## 1.2 THEORETICAL APPROACH

and performing a trace over the phonons gives the spectral density in terms of the autocorrelation of the electron-phonon coupling operators.

$$S_{nm}(\tilde{\omega}) = \int_{-\infty}^{\infty} dt e^{-i\tilde{\omega}t} \langle \hat{V}_{nm}(t) \hat{V}_{mn}(0) \rangle. \quad (1.9)$$

Here,  $\hat{V}_{nm}(t)$  is the electron-phonon coupling term in the Heisenberg representation and  $\langle \dots \rangle$  denotes a thermal average over the vibrational degrees of freedom. The derivation and explicit form for the kernel in Eq. 1.9 is quite lengthy and is given in Ref. [9].

### 1.2.2 Non-Markovian Master Equation and Golden-Rule rates

In Ref. [9], Pereverzev and Bittner derived a non-Markovian, time-convolutionless form of the Pauli master equation (TCLME) for general system described by Eq. 2.7.

$$\frac{dP_n}{dt} = \sum_m W_{nm}(t) P_m(t) - \left( \sum_m W_{mn}(t) \right) P_n(t) \quad (1.10)$$

where the time-dependent rates are given by

$$W_{nm}(\tau) = 2\text{Re} \int_0^\tau dt \langle \hat{V}_{nm}(0) \hat{V}_{mn}(t) \rangle e^{-i\tilde{\omega}_{nm}t}. \quad (1.11)$$

In the limit that  $\tau \rightarrow \infty$ , Eq. 1.11 gives the Fermi's Golden Rule expression for the transition rate,

$$k_{nm} = 2\text{Re} \int_0^\infty dt \langle \hat{V}_{nm}(0) \hat{V}_{mn}(t) \rangle e^{-i\tilde{\omega}_{nm}t}. \quad (1.12)$$

## 1.2 THEORETICAL APPROACH

At this point it is useful to connect the various terms in the phonon-dressed Hamiltonian with specific physical parameters. First, the reorganization energy is given by

$$\lambda_{nm} = \sum_j \frac{(g_{nnj} - g_{mmj})^2}{\omega_j} = \sum_j \hbar \omega_j S_j$$

where the  $\{S_j\}$  are the Huang-Rhys factors for each phonon mode. These are related to the Franck-Condon factor describing the overlap between the  $v_j = 1$  vibronic state in one electronic state with the  $v_j = 0$  vibronic state in the other. Likewise, the energy difference between the renormalized energy gaps is related to the driving force of the state-to-state transition,

$$\Delta E_{nm} = \tilde{\epsilon}_n - \tilde{\epsilon}_m. \quad (1.13)$$

The difficulty in using this approach is that it requires both diagonal ( $g_{nn}$ ) and off-diagonal ( $g_{nm}$ ) derivative couplings between adiabatic states. In the following section, we discuss how we have used the Edmiston-Ruedenberg localization scheme to estimate the couplings[23]. We also present how one can construct a reduced set of harmonic modes that fully capture the electron/nuclear coupling.

### 1.2.3 Parameterization From Quantum Chemistry

In order to obtain the final form of our target Hamiltonian, we assume the diabatic potentials are a good approximation to the actual adiabatic potentials.

When the adiabatic (and diabatic) energy minima are far enough away from the crossing points and the mixing angles between the diabatic and adiabatic states is small, we can use the gradients of the adiabatic potentials to approximate the diabatic potentials. Thus, if we perform calculations

## 1.2 THEORETICAL APPROACH

at the optimized geometry of the final acceptor state (*i. e.* about  $Q_2$  in Fig. 1), we can write the Hamiltonian as

$$H_{dia,e} = \begin{pmatrix} \epsilon_1 & V_{12} \\ V_{21} & \epsilon_2 \end{pmatrix} + \begin{pmatrix} 0 & 0 \\ 0 & 1 \end{pmatrix} \mathbf{g}_{22} \cdot \mathbf{q} + H_{osc}, \quad (1.14)$$

where  $H_{osc}$  is the harmonic oscillator Hamiltonian for the vibrational normal modes. The linear assumption amounts to performing a series expansion of the full, multi-dimensional coupling term and keeping only the lowest order terms. Systematic improvement can be made by including higher-order (e.g. quadratic) off-diagonal couplings. However, this would involve a substantial increase in the complexity of the theory. The linear assumption is reasonable so long as the mixing angle is small, as verified by the benchmark calculations presented below.

We obtain the diabatic couplings  $V_{12}$  and the mixing angle  $\theta$  via ER localization and transform the electronic Hamiltonian from the adiabatic basis to the diabatic basis *viz.*

$$H_{dia} = \begin{pmatrix} \cos \theta & -\sin \theta \\ \sin \theta & \cos \theta \end{pmatrix} \begin{pmatrix} \epsilon_1 & 0 \\ 0 & \epsilon_2 \end{pmatrix} \begin{pmatrix} \cos \theta & \sin \theta \\ -\sin \theta & \cos \theta \end{pmatrix}. \quad (1.15)$$

The diabatic coupling is then given by

$$V_{ab} = \frac{1}{2} \sin 2\theta (\epsilon_2 - \epsilon_1). \quad (1.16)$$

We then diagonalize the electronic part and transform the electron/nuclear coupling back into the adiabatic basis. In doing so, we obtain the Hamiltonian in the form given in Eq. 2.7

$$H = U^T H_{dia} U$$

## 1.2 THEORETICAL APPROACH

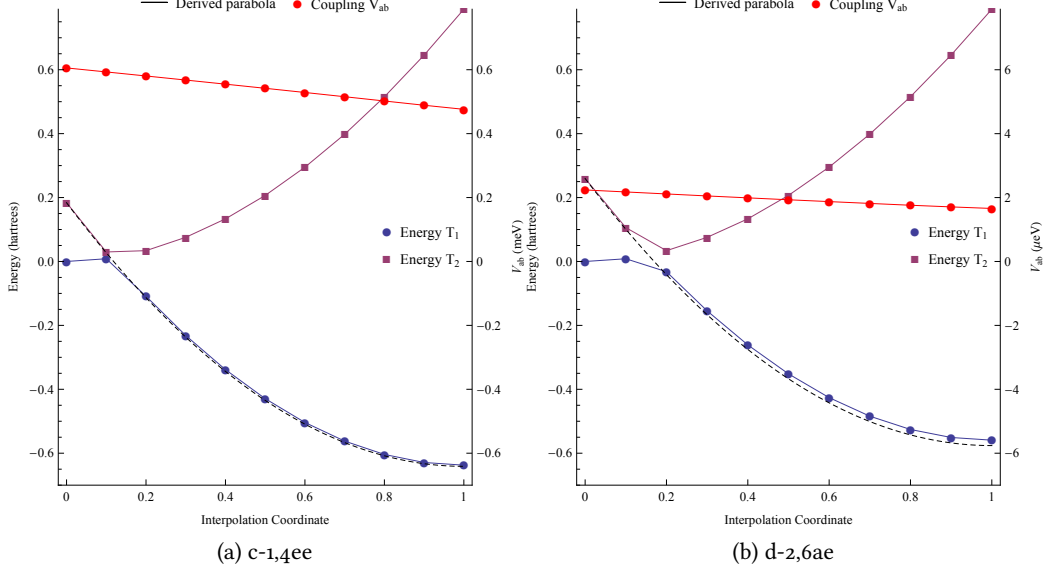


Figure 2: Adiabatic energy curves and off-diagonal couplings computed along an interpolation coordinate between the  $D^* - B - A$  and  $D - B - A^*$  equilibrium geometries.  $V_{ab}$  is the off-diagonal coupling at each point along this coordinate.

$$\begin{aligned}
 &= \begin{pmatrix} E_1 & 0 \\ 0 & E_2 \end{pmatrix} + \begin{pmatrix} \sin^2 \theta & \frac{1}{2} \sin 2\theta \\ \frac{1}{2} \sin 2\theta & \cos^2 \theta \end{pmatrix} \mathbf{g}_{22} \cdot \mathbf{q} \\
 &+ H_{osc}.
 \end{aligned} \tag{1.17}$$

In Fig. 2 we show the adiabatic potential curves and off-diagonal couplings along an interpolation coordinate connecting the equilibrium geometries of the donor and acceptor states for the donor-[d-2,6ae]-acceptor case. The dashed curve gives the parabolic approximation to the lower potential curves. Along this coordinate, the off-diagonal coupling is small and essentially linear and the parabolic approximation provides a good approximation to the actual potential. This indicates that the assumptions in our model Hamiltonian are generally robust for the systems we consider herein.

## 1.3 ENERGY TRANSFER RATES IN DONOR-BRIDGE-ACCEPTOR SYSTEMS

Using the ER localization approach, all parameters needed for our model can be obtained from standard quantum chemical packages. The vertical energies,  $\epsilon_a$  and  $\epsilon_b$  are obtained from single point CI(S) calculations at a given reference geometry. We then project the energy gradients onto the vibrational normal coordinates to obtain the electron-phonon coupling constants. Either the Boys or ER localization scheme can be used to compute the mixing angles for constructing diabatic states. For all calculations shown here we used the qChem 4.0 code and employed the 6-31G(d)\*\* basis set in order to compare our results with Ref. [8].

We benchmark our approach against a series of donor-bridge-acceptor molecules studied by Closs[19, 20, 24]. These cases are significant in that they provided a crucial verification of the Marcus inverted regime. Table 1 and Fig. 3 summarize our results. In addition, we give the diabatic coupling  $V_{ab}$ , reorganization energy  $\lambda$ , and driving force  $\Delta\epsilon$  computed using the Edmiston-Reudenberg (ER) localization method.

In general, our results and those in Ref.[8] agree with each other well and both are comparable to the experimental results which report an estimated error of 10-20% in the rate for each case presented here. Furthermore, all theoretical values were computed in the absence of solvent environment, whereas the experiments were all performed in benzene solvent at a standard temperature. However, there is considerable disagreement between the experimental and theoretical results for the d-2,6ea and methyl (M) bridged cases. For the d-2,6ea bridge, our results are similar to the Marcus theory rates given in Ref. [8]. In this case, the the ER localization gives a small diabatic coupling and it was difficult to obtain converged localized states. In the case of the methyl-bridge, there is a significant change in the geometry between donor and acceptor states. As a result, the potential surfaces are no longer parabolic and the Condon approximation breaks down.[8]

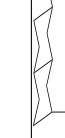
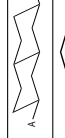
Bridge	Structure	Rates ( $s^{-1}$ )			Marcus theory parameters		
		Expt. Ref. [19, 20]	Marcus Theory Ref. [8]	This work	$\lambda$ (eV)	$\Delta\epsilon$ (eV)	$V_{ab}$ ( $\mu\text{eV}$ )
c-1,3ea		3.3E9	3.9E9	2.2E9	0.823	-0.612	470.1
c-1,3ee		7.7E9	2.1E10	2.8E10	0.810	-0.580	1687.3
c-1,4ea		4.0E7	1.3E7	1.8E7	0.817	-0.604	43.20
c-1,4ee		1.3E9	3.9E9	3.6E9	0.826	-0.642	605.8
d-2,6ae		1.3E5	1.0E4	4.7E4	0.836	-0.577	2.239
d-2,6ea		7.0E5	3.9E4	5.8E4	0.821	-0.609	2.414
d-2,6ee		3.1E6	5.0E6	4.8E6	0.810	-0.581	22.12
d-2,7ae		1.1E7	2.8E7	3.0E7	0.826	-0.605	55.16
d-2,7ea		1.5E7	1.8E7	4.3E7	0.817	-0.605	65.85
d-2,7ee		9.1E7	3.5E8	3.4E8	0.831	-0.648	185.1
M		5.0E10	n.r.	1.2E9	0.896	-0.636	357.0

Table 1: Comparison of triplet-triplet energy transfer rates obtained from our approach, Marcus rates are from Ref.[8] and experimental rates from Refs.[19, 20]. The experimental error is estimated to be 20% in each case studied here. The  $V_{ab}$  are the diabatic couplings obtained using Edmiston-Ruedenberg diabatization. In each case, D = 4-benzophenonyl and A = 2-naphthyl. n.r. = Not Reported.

#### 1.4 DETERMINING THE OPTIMAL ELECTRON-PHONON COUPLING COMPONENTS

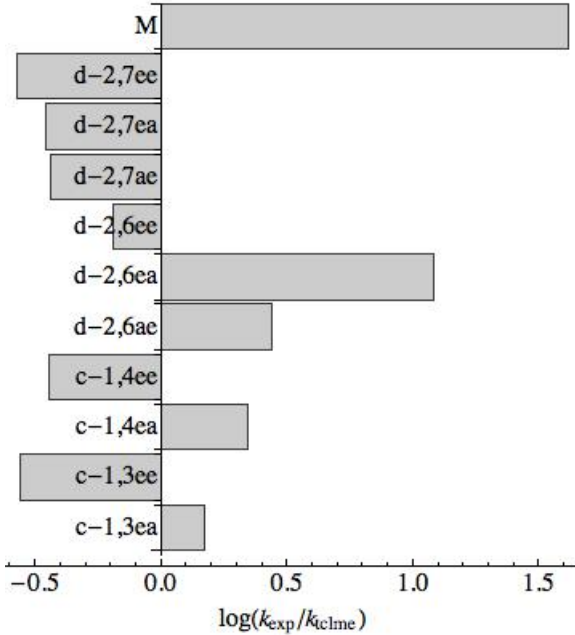


Figure 3: Comparison between predicted (TCLME) rate constants and the experimental rates from Ref.[5]. With exception of the methyl and D-2,6-ea bridged cases, the TCLME results are in good agreement with the experimental results.

#### 1.4 DETERMINING THE OPTIMAL ELECTRON-PHONON COUPLING COMPONENTS

While the Marcus expression is elegant in its simplicity in requiring three parameters that can be obtained experimentally, it masks a wealth of detail that underlie the quantum transition. Central to the theory is that there exists a collective nuclear displacement coordinate that connects the initial geometry of the donor to the final geometry of the acceptor.

Generally speaking, this collective coordinate involves all nuclear degrees of freedom. However, the form of the electronic Hamiltonian in Eq. 2.7 suggests that there exists a subset of motions that are specific modes that capture the majority of the electronic/nuclear coupling and give the

dominant contribution to the collective reaction coordinate. Within the linearized approximation for the electronic/nuclear coupling, we can write a force tensor

$$\mathbf{F} = \begin{pmatrix} \mathbf{g}_{11} & \mathbf{g}_{12} \\ \mathbf{g}_{21} & \mathbf{g}_{22} \end{pmatrix} \quad (1.18)$$

where  $\mathbf{F} \cdot \mathbf{q}$  is the electronic/nuclear coupling term in Eq. 2.7. If we consider each unique element  $\{\mathbf{g}_{11}, \mathbf{g}_{12}, \mathbf{g}_{22}\}$  to be linearly independent, but non-orthogonal force vectors, one can develop a projection operator scheme to parse the  $N$ -dimensional linear vector space spanned by the mass-weighted normal mode vectors into two subspaces: one spanned by three vectors describing the coupling between the electronic states and the other spanned by the remaining  $N - 3$  dimensional space spanned by motions that do not couple the electronic states. This subspace can be generated by defining a projection operator

$$\mathbf{P} = \sum'_{\alpha\beta} (\mathbf{S}^{-1})_{\alpha\beta} \mathbf{g}_\alpha \otimes \mathbf{g}_\beta \quad (1.19)$$

in which the summation is limited to linearly independent vectors. Here  $\mathbf{S}_{\alpha\beta} = \mathbf{g}_\alpha \cdot \mathbf{g}_\beta$ ,  $\otimes$  is outer product, and  $\mathbf{I}$  is unitary operator. This  $N \times N$  matrix projects out all normal modes that are directly coupled to the electronic degrees of freedom and its complement  $\mathbf{Q} = \mathbf{I} - \mathbf{P}$  projects out all modes not directly coupled. By diagonalizing the matrix

$$\mathbf{K} = \mathbf{P} \cdot \Omega \cdot \mathbf{P} + \mathbf{Q} \cdot \Omega \cdot \mathbf{Q} \quad (1.20)$$

we obtain a transformation,  $\mathbf{M}$ , between the normal coordinates and a new set of orthogonal coordinates. Both  $\mathbf{P} \cdot \Omega \cdot \mathbf{P}$  and  $\mathbf{Q} \cdot \Omega \cdot \mathbf{Q}$  are  $N \times N$  matrices. However, for a two-state system, the former will have exactly 3 non-trivial eigenvalues,  $\{\alpha_p\}$ , with corresponding eigenvectors,  $\{M_p\}$ , whereas the latter will have exactly  $N_r = N - 3$  non-trivial eigenvalues,  $\{\alpha_q\}$ , and corresponding

eigenvectors,  $\{M_q\}$ . This the full  $N \times N$  transformation is formed by joining the non-trivial vectors from the two respective subspaces  $\mathbf{M} = \{M_p, M_q\}$ . The transformed electron-phonon coupling constants are given by projecting the couplings in the normal mode basis on to the new basis.

$$\mathbf{g}'_{ab} = \mathbf{M}_p \cdot \mathbf{g}_{ab}. \quad (1.21)$$

By examining the types of molecular motions that compose the  $\mathbf{M}_p$  subspace, we can gain a deeper understanding of the specific classes of internal motion that are directly involved with the electron transfer process. In addition, we can gain a computational advantage since presumably this reduced set of modes give the dominant contribution to the electron-phonon coupling and autocorrelation function given as the kernel in Eq. 2.12.

#### 1.4.1 Lanczos Method

It is crucial to notice that the vectors given in Eq. 2.6 are *not linearly independent*. Consequently, special care must be taken to generate the reduced sub-space. To do so, we use an iterative Lanczos approach taking the normalized vector  $\mathbf{v}_1 = \mathbf{g}_{22}$  as a starting point.

As above, we initialize each step indexed by  $k$ , by defining a projection operator

$$\mathbf{P}_k = \mathbf{v}_k \otimes \mathbf{v}_k \quad (1.22)$$

and its complement  $\mathbf{Q}_k = \mathbf{I} - \mathbf{P}_k$ .  $k$ -th mode. We then project the hessian matrix  $\Omega$  into each subspace *viz.*

$$\Omega_p = \mathbf{P}_k \cdot \Omega \cdot \mathbf{P}_k \quad \& \quad \Omega_q = \mathbf{Q}_k \cdot \Omega \cdot \mathbf{Q}_k \quad (1.23)$$

and diagonalize each to obtain eigenvalues and eigenvectors  $\{\alpha_p, \mathbf{M}_p\}$  and  $\{\alpha_q, \mathbf{M}_q\}$  respectively. As above,  $\Omega_p$  and  $\Omega_q$  are  $N \times N$  matrices. The first set will have a single non-trivial eigenvalue and the second set will have  $N - k$  non-trivial eigenvalues. As above we collect the non-trivial eigenvectors associated with each to form the orthogonal transformation matrix

$$\mathbf{M}_k = \{\mathbf{M}_p, \mathbf{M}_q\}. \quad (1.24)$$

and again transform the full hessian  $\Omega$  into this new vector space to form the  $N \times N$  matrix  $\Omega'$ . At each step in the iteration, the transformed hessian,  $\Omega'$  is in the form of a  $k \times k$  tri-diagonal submatrix in the upper-left part of the matrix and a diagonal submatrix in the lower-right. For example, after  $k = 3$  iterations, one has a Hessian matrix of the form:

$$\Omega' = \begin{pmatrix} \alpha_1 & b_1 & 0 & & & & 0 \\ b_1 & \alpha_2 & b_2 & & & & \\ 0 & b_2 & \alpha_3 & c_{k+1} & c_{k+2} & \cdots & c_N \\ & & c_{k+1} & \alpha_{k+1} & & & 0 \\ & & & c_{k+2} & & \alpha_{k+2} & \\ & & & \vdots & & \ddots & \\ 0 & & c_N & 0 & & & \alpha_N \end{pmatrix}. \quad (1.25)$$

We note that only the  $k$ -th mode is coupled the  $N - k$  remaining modes. Since all of the transformations are orthogonal, diagonalizing  $\Omega'$  at any point returns the original Hessian matrix.

To continue iterating, we take the  $k$ -th row of  $\Omega'$  and zero the first  $k$  elements

$$\mathbf{e} = \{0, \dots, 0, c_{k+1}, c_{k+2}, \dots, c_N\}.$$

This is the coupling between the upper tridiagonal block and the lower diagonal block. We thus obtain a new vector

$$\mathbf{v}_{k+1} = \mathbf{e} \cdot \mathbf{M}$$

which is then reintroduced into the iteration scheme.

At any point along the way, we can terminate the iteration and obtain a reduced set of couplings. Since the Lanczos approach uses the power method for finding the largest eigenvector of a matrix, it converges first upon the vector with the largest electron/nuclear coupling—which we refer to as the “primary mode”. Subsequent iterations produce reduced modes with weaker electron/nuclear couplings and the entire process can be terminated after a few iterations. After  $k$ -steps, the final electron-phonon couplings are then obtained by projecting the original set of couplings (in the normal mode basis) into the final vector space.

For the first iteration,  $\mathbf{v}_1$  is parallel to the bare electron-phonon coupling vector  $g_{22}$  and the associated frequency is  $\mathbf{v}_1 \cdot \Omega \cdot \mathbf{v}_1$ . The subsequent iterations introduce corrections to this via phonon-phonon coupling. For example, for the  $k = 3$  iteration, we would determine the active vector space in terms of the upper-left  $3 \times 3$  block of the matrix in Eq. 1.25.

$$\Omega'_3 = \begin{pmatrix} \alpha_1 & b_1 & 0 \\ b_1 & \alpha_2 & b_2 \\ 0 & b_2 & \alpha_3 \end{pmatrix} \quad (1.26)$$

Diagonalizing  $\Omega'_3$  returns a set of frequencies and associated eigenvectors which are then used to compute the electron-phonon couplings in this reduced active space. After  $N - 1$  iterations,  $\Omega'$  is a fully tridiagonal matrix and diagonalizing this returns the original normal mode basis.

As an illustrative example of our approach, we consider the first few collective modes for the c-1,4ee and d-2,5ae cases. In Fig. 4 we show the projection of the primary coupling mode onto the coordinate frame of each molecule. The vectors indicate the direction of the electron-phonon

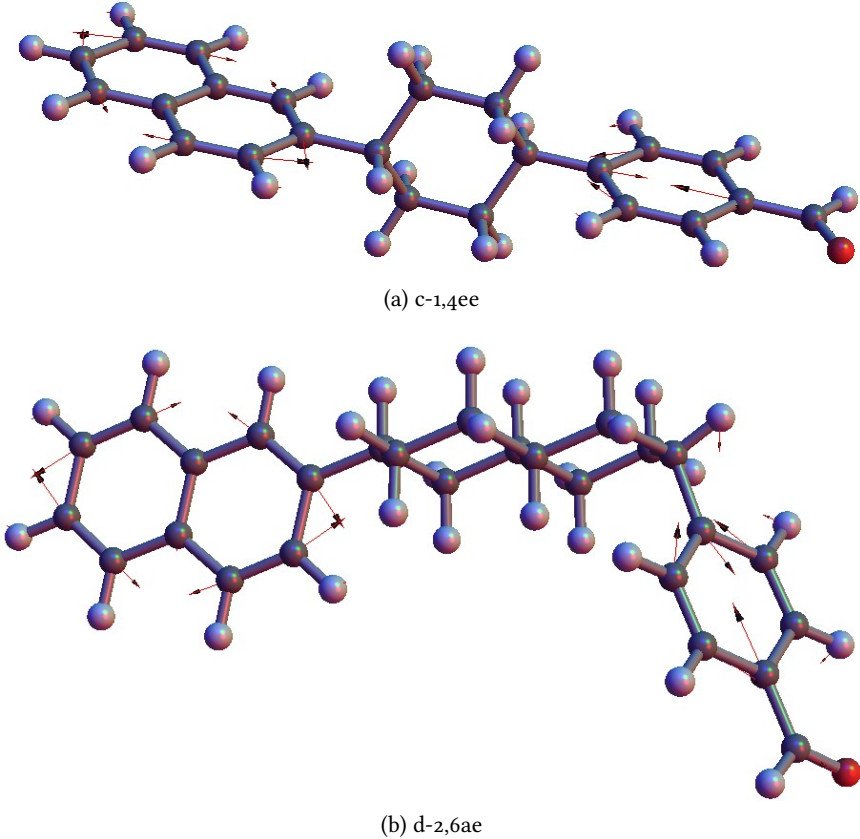


Figure 4: Primary coupling modes for (a)  $c-1,4ee$  and (b)  $d-2,6ae$  projected onto the atomic displacement coordinates.

coupling vectors projected onto the Cartesian displacement vectors of the individual atoms. In each case, the primary coupling mode involves the  $b_{2u}$  in plane C=C stretching motions of the naphthalene donor and the in-plane  $v_8$  (in the Mulliken numbering scheme) ring-squeezing motions of the benzaldehyde acceptor[25]. It is interesting to note that  $^3B_{2u}$  is also the symmetry of the first triplet  $\pi - \pi^*$  excited state in naphthalene [26], Moreover, if we were to approximate benzaldehyde as a  $C_{2v}$  molecule, taking the aldehyde as local site, the resulting first triplet  $\pi - \pi^*$  is the product of a  $b_1$  HOMO and a  $b_1$  LUMO giving a state in the  $a_1$  irreducible representation. This is the same irreducible representation one obtains for the  $v_8$  mode, approximating it as a symmetric

stretching mode. This suggests the existence of underlying symmetry selection or propensity rule in determining the coupling modes.

In order to substantiate our claim that the reduced modes generated by the iterative procedure capture the most important electron-phonon couplings, we consider the convergence of the electron-phonon autocorrelation function used to compute the golden-rule rate constants

$$C(t) = \langle \hat{V}_{nm}(t) \hat{V}_{nm}(0) \rangle \quad (1.27)$$

with respect to the number of reduced modes. We can this term exactly using all  $N$  vibrational modes of the molecule and compare to the results obtained using a subset of modes.

In Fig. 5 we examine the convergence of  $C(t)$  with respect to number of reduced modes for the c-1,4ee and d-2,6ae cases. In both cases, only a handful of reduced modes (4 for c-1,4ee and 15 for d-2,6ae) is needed to accurately track the correlation function for the first 10 fs. For comparison, d-2,6ae has 162 normal modes and c-1,4ee has 132 normal modes. For the primary mode approximation, the recursions appear every 23 fs and are suppressed by the addition of more reduced modes to the calculation. The 23 fs recursion time corresponds to the period of the single reduced mode:  $\omega_1 = 0.18\text{eV}$  ( $1450\text{ cm}^{-1}$ ). For the d-2,6ae case, including 15 modes is sufficient to fully suppress the recursion time to beyond 100 fs. For purposes of computing golden rule rate constants, the Markov limit is reached when  $C(t) \rightarrow 0$ . For the cases at hand, this is well before the first recursion seen in Fig. 5.

While it is surprising that only a few reduced modes are needed to converge the coupling correlation function, only a single mode is necessary to accurately compute the golden-rule rate constant. In Fig. 6 we compare the exact rate constant (using all modes) and rate constants computed

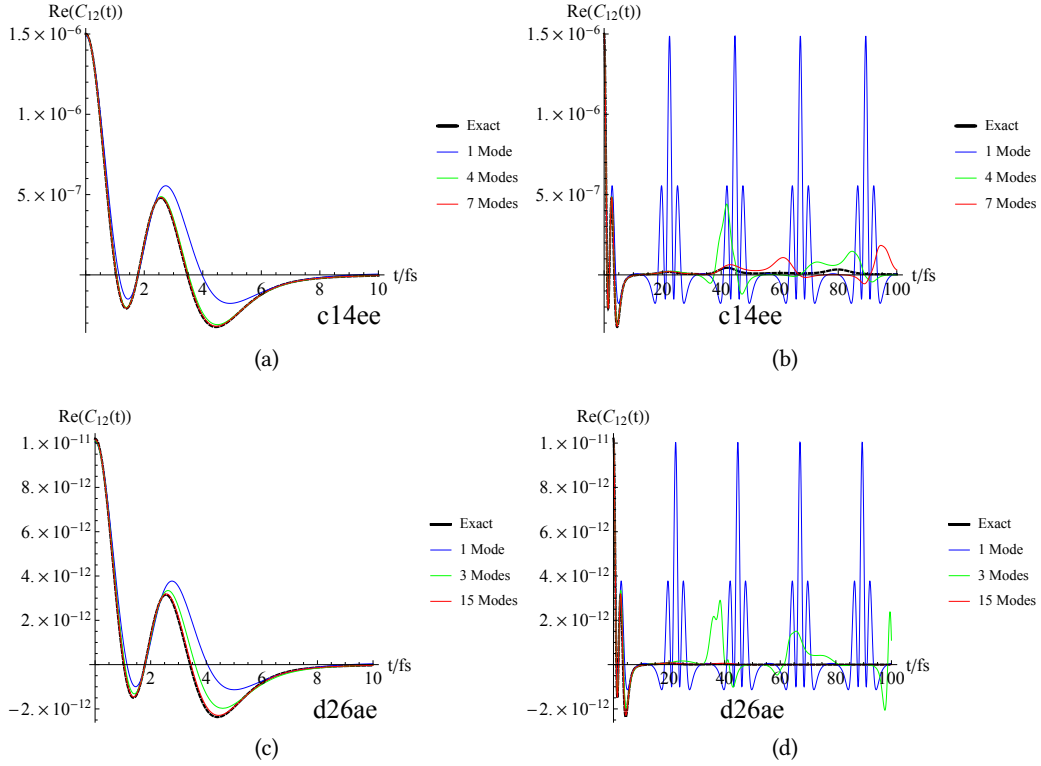


Figure 5: Convergence of the electronic coupling autocorrelation function (Eq. 1.27) with respect to number of reduced modes.

using only the first mode generated by the Lanczos iterations. In the first case represented by the blue points, we approximate the reorganization energy as

$$\lambda_{nm} \approx \frac{g_1^2}{\omega_1}$$

where  $g_1$  and  $\omega_1$  are the coupling and frequency of the first reduced mode. This simple approximation does a superb job compared to the numerically exact rate obtained using all modes and all couplings. On average, the error between the exact and approximate rate is 2% over the entire series of model donor-bridge-acceptor systems considered. The red points represent rates computed using the first reduced mode, but use the exact reorganization energy. Here, the agreement is almost perfect for

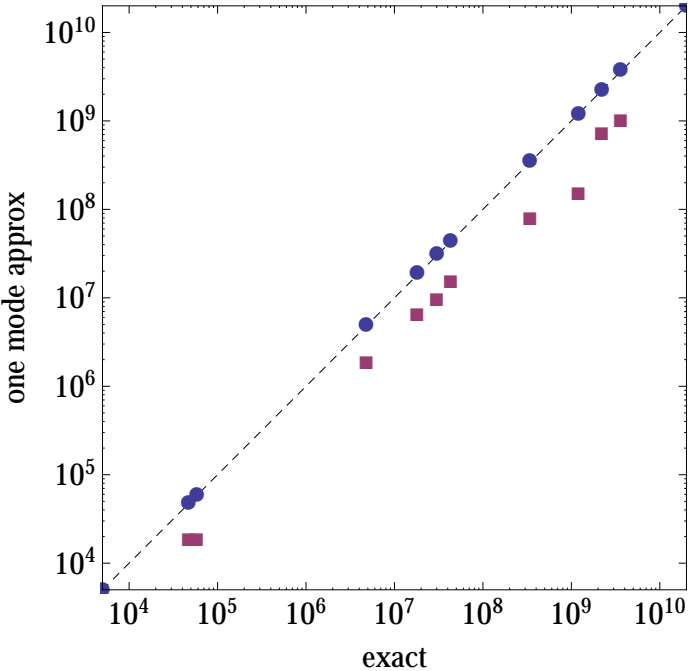


Figure 6: Comparison between exact rate constant and its primary mode approximation. The blue points correspond to rates computed using only the primary mode and the reorganization energy for only that mode. The red points use the primary mode and the exact renormalized energies.

the two fastest rates corresponding to d-2,6ae and d-2,6ea. However, on average this approximation is off by a factor of 3 compared to the exact rate. For the methyl-bridged case, the rate is off by a factor of 8.. This implies that the first reduced mode indeed captures the majority of the electron-phonon coupling and provides a unique description of the Marcus reaction coordinate.

In Table 2 we tabulate the frequencies and electron-phonon coupling constant for the first reduced mode for each test case. Uniformly, these modes correspond to ring breathing motions on the donor and acceptor as illustrated in Fig. 4. As seen in this figure, coupling mode does not involve normal modes localized on the bridge species. Moreover, the magnitude of the electronic coupling carried by this mode is uniformly around 0.37 eV and independent of the bridge. No single normal mode captures all of the electronic coupling. This is evidenced by the fact that the magnitude of

### 1.5 DISCUSSION

bridge	$\omega_1$ (eV)	$ g_1 $ (eV)	$ g_{max} $ (eV)
c-1,3ea	0.184	0.367	0.159
c-1,3ee	0.185	0.365	0.162
c-1,4ea	0.185	0.367	0.166
c-1,4ee	0.185	0.370	0.171
d-2,6ae	0.185	0.367	0.159
d-2,6ea	0.185	0.367	0.142
d-2,6ee	0.185	0.365	0.143
d-2,7ae	0.184	0.366	0.165
d-2,7ea	0.185	0.367	0.142
d-2,7ee	0.185	0.370	0.149
M	0.184	0.366	0.160

Table 2: Frequencies and dimensionless electron-phonon couplings for the first reduced mode for each model system. The last column gives the absolute value of the largest coupling constant within the normal mode basis.

the electronic coupling carried by the first reduced mode is over twice that of the largest coupling along a single normal mode.

### 1.5 DISCUSSION

We present here a new approach for computing intramolecular energy and charge transfer rates by combining a time-convolutionless master equation approach for state to state population transfer as parameterized by a rigorous quantum chemical approach. The approach is robust over a wide range of model systems and generally gives good agreement compared to experimental rates and Marcus theory rates. Only in cases where the parabolic approximation to the diabatic potentials breaks down or when the ER localization method fails to converge is the agreement with the experimental rates less than satisfactory.

## 1.5 DISCUSSION

A crucial part of our analysis is the identification of a subset of collective modes that contain the electron-phonon couplings. Moreover, we show that there exists a unique mode—the “primary mode”, determined via an iterative approach, along which the off-diagonal electron-phonon coupling is maximized. Using only the primary mode mode as input to our golden-rule rate expression, we obtain excellent agreement (to within 2% on average over all of the donor-bridge-acceptor systems studied here) when compared to an exact evaluation using all normal modes. One can visualize the primary mode by projecting it on to the nuclear displacement vectors and gain insight into the coupled electronic/nuclear motions that underlie an electronic transition. Our analysis also suggests that the primary mode reflects the irreducible representations of the donor and acceptor excited states.

## BIBLIOGRAPHY

---

- [1] Marcus, R. A. On the Theory of Oxidation-Reduction Reactions Involving Electron Transfer. I. *J. Chem. Phys.* **1956**, *24*, 966–978.
- [2] Marcus, R. A. On the Theory of Electron-Transfer Reactions. VI. Unified Treatment for Homogeneous and Electrode Reactions. *J. Chem. Phys.* **1965**, *43*, 679.
- [3] Marcus, R. A. Electron transfer reactions in chemistry. Theory and experiment. *Rev. Mod. Phys.* **1993**, *65*, 599–610.
- [4] Dexter, D. L. A Theory of Sensitized Luminescence in Solids. *J. Chem. Phys.* **1953**, *21*, 836–850.
- [5] Miller, J.; Calcaterra, L.; Closs, G. Intramolecular long-distance electron transfer in radical anions. The effects of free energy and solvent on the reaction rates. *J. Am. Chem. Soc.* **1984**, *106*, 3047–3049.
- [6] Subotnik, J. E.; Yeganeh, S.; Cave, R. J.; Ratner, M. A. Constructing diabatic states from adiabatic states: Extending generalized Mulliken–Hush to multiple charge centers with Boys localization. *J. Chem. Phys.* **2008**, *129*, 244101.
- [7] Subotnik, J. E.; Cave, R. J.; Steele, R. P.; Shenvi, N. The initial and final states of electron and energy transfer processes: Diabatization as motivated by system-solvent interactions. *J. Chem. Phys.* **2009**, *130*, 234102–234102.
- [8] Subotnik, J. E.; Vura-Weis, J.; Sodt, A. J.; Ratner, M. A. Predicting accurate electronic energy transfer rates via Marcus theory and Edmiston-Ruedenberg localized diabatization. *J. Phys. Chem. A* **2010**, *114*.

## Bibliography

- [9] Pereverzev, A.; Bittner, E. R. Time-convolutionless master equation for mesoscopic electron-phonon systems. *J. Chem. Phys.* **2006**, *125*, 104906.
- [10] Tamura, H.; Ramon, J. G. S.; Bittner, E. R.; Burghardt, I. Phonon-Driven Ultrafast Exciton Dissociation at Donor-Acceptor Polymer Heterojunctions. *Physical Review Letters* **2008**, *100*, APS.
- [11] Tamura, H.; Bittner, E. R.; Burghardt, I. Exciton dissociation at donor-acceptor polymer heterojunctions: Quantum nonadiabatic dynamics and effective-mode analysis. *J. Chem. Phys.* **2007**, *126*, 021103.
- [12] Bittner, E. R.; Silva, C. Noise-induced quantum coherence drives photo-carrier generation dynamics at polymeric semiconductor heterojunctions. *Nat. Comm.* **2014**, *5*, 3119.
- [13] Singh, J.; Bittner, E. R.; Beljonne, D.; Scholes, G. D. Fluorescence Depolarization in MEH-PPV: Sites vs. Eigenstates Hopping. *J. Chem. Phys.* **2009**, *131*, 194905.
- [14] Cederbaum, L.; Gindensperger, E.; Burghardt, I. Short-Time Dynamics Through Conical Intersections in Macrosystems. *Phys. Rev. Lett.* **2005**, *94*, 113003.
- [15] Gindensperger, E.; Burghardt, I.; Cederbaum, L. S. Short-time dynamics through conical intersections in macrosystems. I. Theory: Effective-mode formulation. *J. Chem. Phys.* **2006**, *124*, 144103.
- [16] Gindensperger, E.; Burghardt, I.; Cederbaum, L. S. Short-time dynamics through conical intersections in macrosystems. II. Applications. *J. Chem. Phys.* **2006**, *124*, 144104.
- [17] Cederbaum, L. S.; Gindensperger, E.; Burghardt, I. Short-Time Dynamics Through Conical Intersections in Macrosystems. *Phys. Rev. Lett.* **2005**, *94*, 113003.
- [18] Pereverzev, A.; Bittner, E. R.; Burghardt, I. Energy and charge-transfer dynamics using projected modes. *J. Chem. Phys.* **2009**, *131*, 034104.

## Bibliography

- [19] Closs, G. L.; Piotrowiak, P.; MacInnis, J. M.; Fleming, G. R. Determination of long-distance intramolecular triplet energy-transfer rates. Quantitative comparison with electron transfer. *J. Am. Chem. Soc.* **1988**, *110*, 2652–2653.
- [20] Closs, G. L.; Johnson, M. D.; Miller, J. R.; Piotrowiak, P. A connection between intramolecular long-range electron, hole, and triplet energy transfers. *J. Am. Chem. Soc.* **1989**, *111*, 3751–3753.
- [21] Grover, M. K.; Silbey, R. Exciton–Phonon Interactions in Molecular Crystals. *J. Chem. Phys.* **1970**, *52*, 2099–2108.
- [22] Rice, M. J.; Gartstein, Y. N. Excitons and interband excitations in conducting polymers based on phenylene. *Phys. Rev. Lett.* **1994**, *73*, 2504–2507.
- [23] Edmiston, C.; Ruedenberg, K. Localized Atomic and Molecular Orbitals. *Rev. Mod. Phys.* **1963**, *35*, 457–464.
- [24] Closs, G. L.; Miller, J. R. Intramolecular long-distance electron transfer in organic molecules. *Science* **1988**, *240*, 440–447.
- [25] Silva, C. R.; Reilly, J. P. Theoretical Calculations on Excited Electronic States of Benzaldehyde and Observation of the  $S_2 \leftarrow S_0$  Jet-Cooled Spectrum. *J. Phys. Chem.* **1996**, *100*, 17111–17123.
- [26] Ågren, H.; Minaev, B. F.; Knuts, S. Response Theory Studies of Triplet-State Spectra and Radiative Lifetimes of Naphthalene, Quinoxaline, and Phthalazine. *J. Phys. Chem.* **1994**, *98*, 3943–3949.

# 2

## CHAPTER 3

---

### 2.1 INTRODUCTION

One of the most important and fundamental processes in chemical dynamics is that of energy and charge transfer between molecular species. The mechanism itself is highly quantum mechanical in nature and involves strong coupling between nuclear and electronic degrees of freedom. The seminal model for the calculation of the transfer rate for this process was developed by Marcus in the 1950's[1–3]

$$k_{\text{Marcus}} = \frac{2\pi}{\hbar} |V_{ab}|^2 \frac{1}{\sqrt{4\pi k_B T \lambda}} e^{-(\lambda + \Delta G^\circ)^2 / 4\lambda k_B T}, \quad (2.1)$$

which relates the Fermi golden-rule transition rate,  $k_{\text{Marcus}}$  to the thermodynamic driving force  $\Delta G^\circ$  and the reorganization energy  $\lambda$ . One of the most striking predictions of this theory is that as the free energy difference between the final and initial state increases, the transition rate reaches its maximum, and further increases in the energy off-set leads to slower transition rates. This “inverted regime” was confirmed by Closs and Miller[4–6] nearly 30 yrs later.

Numerous improvements to the Marcus model have been presented over the years and a detailed exploration of each is well beyond the scope of this work. Aside from the electronic coupling,  $V_{ab}$ , the other terms in the expression of rate constant arise from a semi-classical approximation to the overlap between the initial vibrational states of the donor and the the final states of the acceptor

---

o Part of this chapter has been published in Xunmo Yang and E. R. Bittner, The Journal of Chemical Physics **142**, 244114 (2015)

## 2.1 INTRODUCTION

state. It suffices to say that most of the efforts focus upon incorporating more molecular-level detail into the couplings and vibrational modes used in computing these terms.

A number of years ago, we developed a time-convolutionless master equation approach (TCLME) for computing state-to-state rate in which the coupling between states depends upon the nuclear coordinates[7]. This approach incorporates a fully quantum mechanical treatment of both the nuclear and electronic degrees of freedom and recovers the Marcus rate equation in the semiclassical limit. The model itself is parameterized by the vibrational normal mode frequencies, the electronic energies, and energy derivatives at a reference configuration obtained from *ab initio* quantum chemistry computations. The approach has been intensively used and testified by our group to compute state-to-state transition rates in semi-empirical models for organic semiconducting light-emitting diode and photovoltaics [8–11]. Central to our work here is the use of a mode-projection scheme which parses out a reduced set of nuclear motions primarily coupled to the quantum transition. We refer to the modes identified early in the iterative process as the “primary Lanczos modes” or PLMs.

Using the TCLME approach, we recently investigated triplet-triplet excitation energy transfer between a naphthalene donor and a benzaldehyde acceptor linked by a variety of bridging units as shown in Fig. 7. [12] Such systems were the basis of a classic series of experiments by Closs and Miller[4–6] which verified the existence of the Marcus inverted regime. In Ref. [12] we showed that both the autocorrelation function of the electronic coupling operators and the total transfer rate constant calculated using TCLME approach with only PLMs provide an excellent approximation to the exact correlation functions and rate constants computed using all normal modes, as well as to the experimental and recent theoretical values for the transfer rates.[13]

In this paper we analyze the symmetry of PLMs in model donor-bridge-acceptor systems as projected onto the local vibrational modes of the donor (benzaldehyde) and acceptor (naphthalene) moieties. By constructing the local modes from the dominant normal modes in the projection, one can deduce a relation between the PLMs, fragment modes, and normal modes for the entire

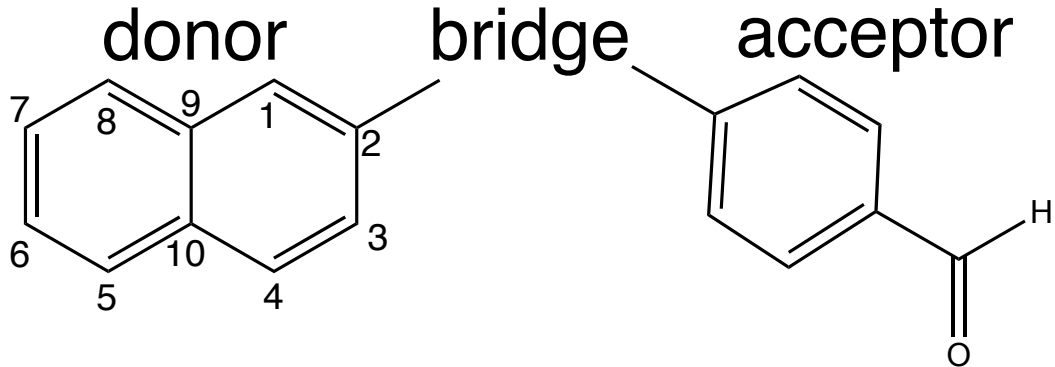


Figure 7: Molecular structure of naphthalene donor and a benzaldehyde acceptor linked by various bridging units.

molecule. The structure of this paper is as follows. We begin by reviewing the TCLME approach and how one generates the PLMs. We then discuss the symmetry of PLMs and their relation to a linear coordinate linking the initial/donor geometry to the final/acceptor geometry of the molecule.

## 2.2 THEORETICAL MODEL

Our method was detailed in Ref.[12] but to be self-contained, we briefly present it here.

### 2.2.1 Hamiltonian and Parameterization

We start with the generic form for the diabatic Hamiltonian, describing two electronic states coupled with  $N$  normal modes:

$$H_{dia} = \begin{pmatrix} \epsilon_1 & V_{12} \\ V_{21} & \epsilon_2 \end{pmatrix} + \begin{pmatrix} g_{11} & g_{12} \\ g_{21} & g_{22} \end{pmatrix} \cdot \mathbf{q} + \frac{\mathbf{p}^2}{2} + \frac{1}{2} \mathbf{q}^T \cdot \Omega \cdot \mathbf{q}.$$

(2.2)

Here, the first term contains the electronic energies,  $\epsilon_1$  and  $\epsilon_2$  computed at a reference geometry—typically that of the donor or acceptor state.  $V_{ij}$  is the diabatic coupling between them. The second term represents the linear coupling between the electronic and nuclear degrees of freedom given in terms of the mass-weighted normal coordinates  $\mathbf{q}$ . The diagonal terms give the diabatic displacement forces between the reference geometry and the two states. The remaining two terms correspond to the harmonic motions of the nuclear normal modes, given here in mass-weighted normal coordinates. In the normal mode basis,  $\Omega$  is diagonal with elements corresponding to the normal mode frequencies,  $\omega_j^2$ .

If we choose one of the states as the reference state, then either  $\mathbf{g}_{11}$  or  $\mathbf{g}_{22}$  will vanish. We further assume Condon approximation to neglect  $\mathbf{g}_{12}$  and  $\mathbf{g}_{21}$ . Now the Hamiltonian is simplified to

$$H_{dia} = \begin{pmatrix} \epsilon_1 & V_{12} \\ V_{21} & \epsilon_2 \end{pmatrix} + \begin{pmatrix} 0 & 0 \\ 0 & 1 \end{pmatrix} \mathbf{g}_{22} \cdot \mathbf{q} + H_{osc}, \quad (2.3)$$

where  $H_{osc}$  is the harmonic oscillator Hamiltonian for the vibrational normal modes.

To calculate transition rate, we transform to adiabatic representation. It is done via Edmiston-Ruendenberg (ER) localization[13] implemented in Q-Chem and the electronic Hamiltonians on adiabatic and diabatic basis are related by the mixing angle  $\theta$ .

$$H_{dia,e} = \begin{pmatrix} \cos \theta & -\sin \theta \\ \sin \theta & \cos \theta \end{pmatrix} \begin{pmatrix} \epsilon_1 & 0 \\ 0 & \epsilon_2 \end{pmatrix} \begin{pmatrix} \cos \theta & \sin \theta \\ -\sin \theta & \cos \theta \end{pmatrix}. \quad (2.4)$$

The diabatic coupling is then given by

$$V_{12} = \frac{1}{2} \sin 2\theta (\epsilon_2 - \epsilon_1). \quad (2.5)$$

## 2.2 THEORETICAL MODEL

The full adiabatic Hamiltonian reads:

$$\begin{aligned}
 H &= U^T H_{dia} U \\
 &= \begin{pmatrix} E_1 & 0 \\ 0 & E_2 \end{pmatrix} + \begin{pmatrix} \sin^2 \theta & \frac{1}{2} \sin 2\theta \\ \frac{1}{2} \sin 2\theta & \cos^2 \theta \end{pmatrix} \mathbf{g}_{22} \cdot \mathbf{q} \\
 &\quad + H_{osc}.
 \end{aligned} \tag{2.6}$$

where the electronic part is in the adiabatic basis with eigenenergies  $E_1$  and  $E_2$  at certain reference geometry. The nuclear normal modes are described by  $H_{osc}$  whereas  $\theta$  is the mixing angle between two states.

To parametrize our Hamiltonian, we assume the diabatic are a good approximation to the actual adiabatic potentials. This allows us to use the gradients of the adiabatic potentials to approximate the diabatic potentials. This approximation is valid when the adiabatic (and diabatic) energy minima are far enough away from the crossing points and the mixing angles between the diabatic and adiabatic states is small. Thus, all parameters in Eq. 2.6 can be obtained from standard quantum chemical computations. As in our previous work, we use the Q-Chem 4.0 package to obtain the vertical energies from single point CI(S) calculations with 6-31G\*\* basis set at a given reference geometry. We then project the energy gradients onto the vibrational normal coordinates

Our group has shown that the dynamics of Hamiltonian in the form of Eq. 2.6 can be expressed in a time-convolutionless master equation [7]. The derivation is lengthy so we present it briefly.

## 2.2 THEORETICAL MODEL

### 2.2.2 Transition Rate and Autocorrelation

We start from a more general Hamiltonian:

$$H = \begin{pmatrix} \epsilon_1 & 0 \\ 0 & \epsilon_2 \end{pmatrix} + \begin{pmatrix} \mathbf{g}_{11} & \mathbf{g}_{12} \\ \mathbf{g}_{21} & \mathbf{g}_{22} \end{pmatrix} \cdot \mathbf{q} + \frac{\mathbf{p}^2}{2} + \frac{1}{2} \mathbf{q}^T \cdot \Omega \cdot \mathbf{q} \quad (2.7)$$

then perform a polaron transform using the unitary transformation [7, 14, 15].

$$\begin{aligned} U &= e^{-\sum_n i \frac{g_{nni}}{\hbar\omega_i} |n\rangle\langle n| (a_i^\dagger - a_i)} \\ &= \sum_n |n\rangle\langle n| e^{-\sum_i i \frac{g_{nni}}{\hbar\omega_i} (a_i^\dagger - a_i)} \end{aligned} \quad (2.8)$$

under which the transformed Hamiltonian is written in terms of the diagonal elements

$$\tilde{H}_0 = U^{-1} H_0 U = \sum_n \tilde{\epsilon}_n |n\rangle\langle n| + \sum_i \omega_i a_i^\dagger a_i, \quad (2.9)$$

with the renormalized electronic energies,

$$\tilde{\epsilon}_n = \epsilon_n - \sum_i \frac{g_{nni}^2}{\hbar\omega_i}, \quad (2.10)$$

and off-diagonal terms,

$$\hat{V}_{nm} = \sum_i g_{nmi} \left( a_i^\dagger + a_i - \frac{2g_{nni}}{\hbar\omega_i} \right) e^{\sum_j \frac{(g_{nnj} - g_{mmj})}{\hbar\omega_j} (a_j^\dagger - a_j)}. \quad (2.11)$$

After lengthy derivation we get the autocorrelation function in the Heisenberg representation

$$C_{nm}(t) = \langle \hat{V}_{nm}(t) \hat{V}_{mn}(0) \rangle,$$

## 2.2 THEORETICAL MODEL

where  $\langle \cdots \rangle$  denotes a thermal average over the vibrational degrees of freedom. Using this approach, the golden-rule rates are given by

$$k_{nm} = \lim_{\tau \rightarrow \infty} 2\text{Re} \int_0^\tau dt \langle \hat{V}_{nm}(0) \hat{V}_{mn}(t) \rangle e^{-i\tilde{\omega}_{nm} t}. \quad (2.12)$$

In a practical sense, we take  $\tau$  to be some finite time at which the autocorrelation function  $C(t)$  has relaxed to zero.

Later, we will use the  $C_{nm}(t)$  to benchmark the convergence of our model with respect to the number of nuclear modes included in constructing the electronic coupling operator,  $V_{nm}(t)$ . For our purposes here, an “exact” calculation involves including all nuclear vibrational modes. In our previous work we showed that both  $C(t)$  and the total transfer rate constant,  $k_{nm}$  calculated using only the first few projected modes provide an excellent agreement with the exact quantities computed using the full set of normal modes, as well as the experimental rates, when parameterized using accurate quantum chemical data.[12]

### 2.2.3 Constructing Primary Lanczos Modes

The linear coupling parameter  $g_{22}$  in Eq. 2.6 defines a force along a vector connecting the initial and final equilibrium geometries of the molecule. This vector, along with the diabatic mixing angle can be obtained from quantum chemistry using the ER localization scheme to approximate the donor and acceptor states. By analyzing this force we can gain the insight into the dynamics of the transition as well as open an avenue for developing improved approximations for transition rates. In our previous work [12], we presented a Lanczos-base ranking algorithm that project out a series of nuclear displacements that are most important for the transition. We refer to the highest-ranked mode identified by the algorithm as the “primary Lanczos mode” (PLM). The process of finding the

## 2.2 THEORETICAL MODEL

PLMs is initiated by defining the vector  $\mathbf{v}_1 = \mathbf{g}_{22}$ . At each step indexed by  $k$ , we define a projection operator

$$\mathbf{P}_k = \mathbf{v}_k \otimes \mathbf{v}_k \quad (2.13)$$

and its complement  $\mathbf{Q}_k = \mathbf{I} - \mathbf{P}_k$ . We also construct

$$\mathbf{P} = \sum_k \mathbf{P}_k \quad (2.14)$$

as the total projection operator for all  $k \leq N$  modes. We then project the hessian matrix  $\Omega$  into each subspace *viz.*

$$\Omega_p = \mathbf{P}_k \cdot \Omega \cdot \mathbf{P}_k \quad \& \quad \Omega_q = \mathbf{Q}_k \cdot \Omega \cdot \mathbf{Q}_k \quad (2.15)$$

and diagonalize each to obtain eigenvalues and eigenvectors  $\{\alpha_p, \mathbf{M}_p\}$  and  $\{\alpha_q, \mathbf{M}_q\}$  respectively.  $\Omega_p$  and  $\Omega_q$  are  $N \times N$  matrices. The first set of these will have a single non-trivial eigenvalue and the second set will have  $N - k$  non-trivial eigenvalues. We then collect the non-trivial eigenvectors associated with each to form the orthogonal transformation matrix

$$\mathbf{M}_k = \{\mathbf{M}_p, \mathbf{M}_q\}. \quad (2.16)$$

and again transform the full hessian  $\Omega$  into this new vector space to form the  $N \times N$  matrix  $\Omega'$ . At each step in the iteration, the transformed hessian,  $\Omega'$  is in the form of a  $k \times k$  tri-diagonal submatrix in the upper-left part of the matrix and a diagonal submatrix in the lower-right.

In Fig. 8 we show the PLMs for the intramolecular triplet energy transfer within two representative donor-bridge-acceptor molecules from our study, termed c14ee and d26ae. In both cases, triplet energy is transferred from a benzaldehyde (BZ) donor group to a naphthyl- acceptor group.

## 2.2 THEORETICAL MODEL

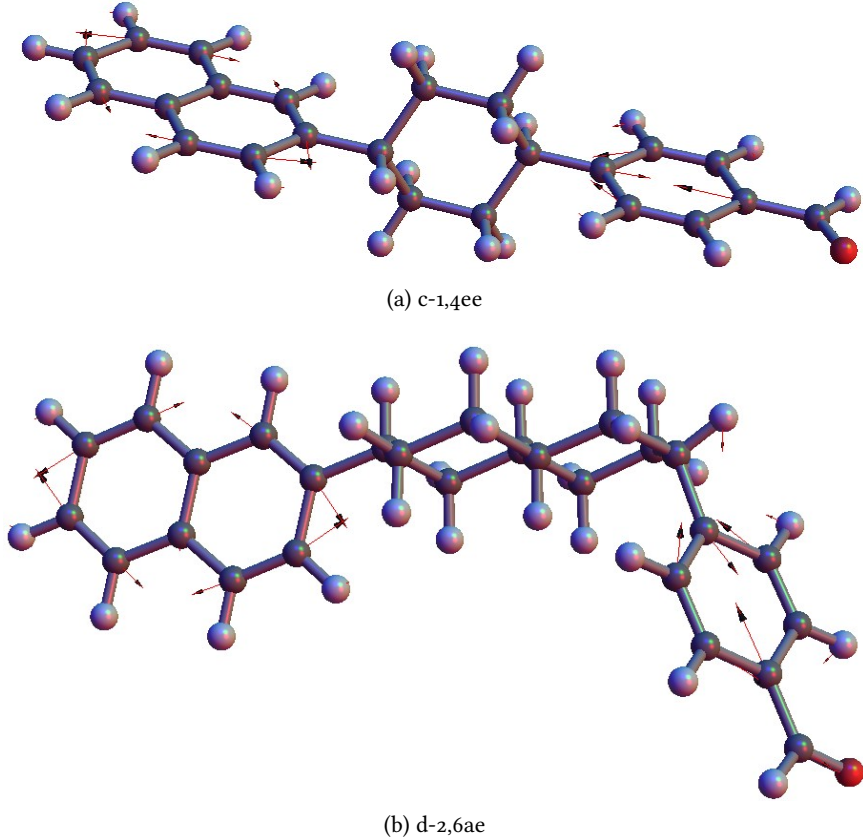


Figure 8: Primary Lanczos modes for (a) c14ee and (b) d26ae projected onto the atomic displacement coordinates. The frequencies for both these are at 0.185 eV ( $1490 \text{ cm}^{-1}$ ), a typical  $C = C$  stretching frequency for arene systems.

Several observations can be made from Fig. 8 concerning the primary Lanczos modes for these donor-bridge-acceptor systems. First, there is negligible contribution from the bridging unit. This is not surprising since the transitions involve electronic energy transfer between  $\pi$ -orbitals localized on the donor and acceptor moieties. Since the bridges in these cases are not conjugated, there is very weak electronic coupling between the D/A groups and the bridge itself. Hence, to a good approximation, the electronic contribution from the bridge can be effectively ignored, it simply serves to hold the donor and acceptor in fixed relative positions. Secondly, the displacement vectors on donor and acceptor moieties are very much akin to totally symmetric normal modes of the

### 2.3 SYMMETRY OF THE PRIMARY LANCZOS MODES

corresponding moieties, and do not correspond any single normal vibrational mode of the whole molecule.

In the next two Sections, we explore the role of symmetry in detail. We first project the PLMs onto the normal modes of both the donor or acceptor moieties and onto entire molecules (donor-bridge-acceptor). Using these reduced PLMs we compute rate constants and compare to the numerically exact results obtained using the full modes. Then we do a similar set of projections using simply the geometric change from initial to final configurations to explore the relation between the PLMs and geometry.

### 2.3 SYMMETRY OF THE PRIMARY LANCZOS MODES

Fig. 9 shows the projection of the PLMs onto the local vibrational modes of D/A moieties in molecules of c14ee and d26ae. In each case, we label the dominant contributions by the irreducible representation (IR) of the moiety. The normal mode basis is generated as follows: first, we take the geometry of donor or acceptor moiety and add the necessary hydrogens. Then the  $D_{2h}$  symmetry is applied to naphthalene using GaussView 5. The benzaldehyde moiety is unchanged because it has very low symmetry:  $C_s$  if planar and  $C_1$  other wise.

If one treats the aldehyde group as a local site, one can classify the ring-motions of benzaldehyde in terms of the  $C_{2v}$  irreducible representations. As a result, the assigned irreducible representations are exact for naphthalene but approximate for benzaldehyde. We then assign a weight to each mode viz.

$$w_i = \frac{\left\langle \vec{M}_i | \overrightarrow{PLM} \right\rangle^2}{\sqrt{\sum_i \left\langle \vec{M}_i | \overrightarrow{PLM} \right\rangle^2}}$$

where  $\vec{M}_i$  is the displacement vector of the  $i$ th normal mode. The symmetrization of naphthalene introduces another problem in that the projection depends on the orientation of the basis vectors.

### 2.3 SYMMETRY OF THE PRIMARY LANCZOS MODES

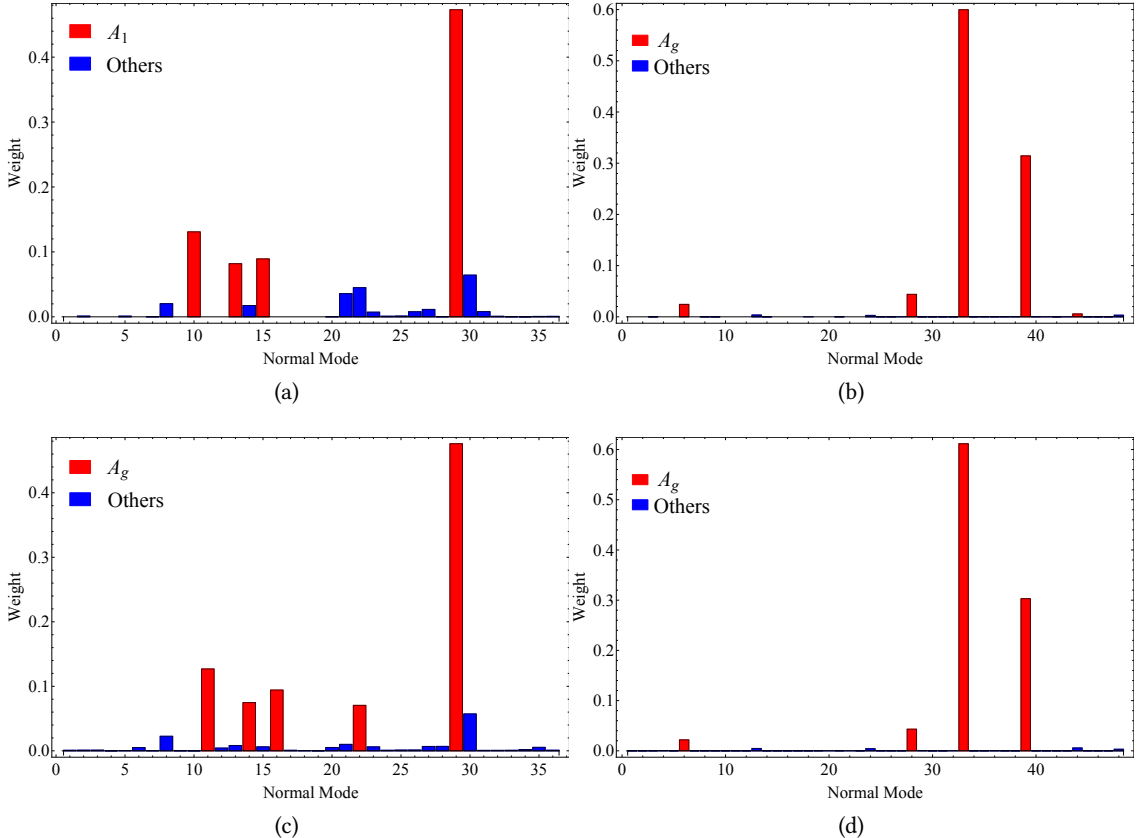


Figure 9: Projection of PLMs onto (a) benzaldehyde in c14ee (b) symmetrized naphthalene in c14ee, (c) benzaldehyde in d26ae and (d) symmetrized naphthalene in d26ae. The normal modes are listed from low to high frequency and the irreducible representations of the dominant modes are color-coded. The assigned IRs for naphthalene are exact whereas the IRs are only approximate for benzaldehyde.

Thus, we orient the original and symmetrized frames by first aligning the center of masses and then minimize the RMS displacement between atoms. Analyzing the projections it becomes clear that in all cases, the dominant components belong to totally symmetric  $A_g$  or  $A_1$  irreducible representations, in agreement with the intuitive observations from Fig. 8.

This behavior is not unique for the naphtyl-bridge-benzaldehyde system. To see this, we repeated the analysis using various acceptor groups as shown in Fig. 10. together with their PLMs and correlation functions for different numbers of projected modes. For both molecules, with 4 projected

### 2.3 SYMMETRY OF THE PRIMARY LANCZOS MODES

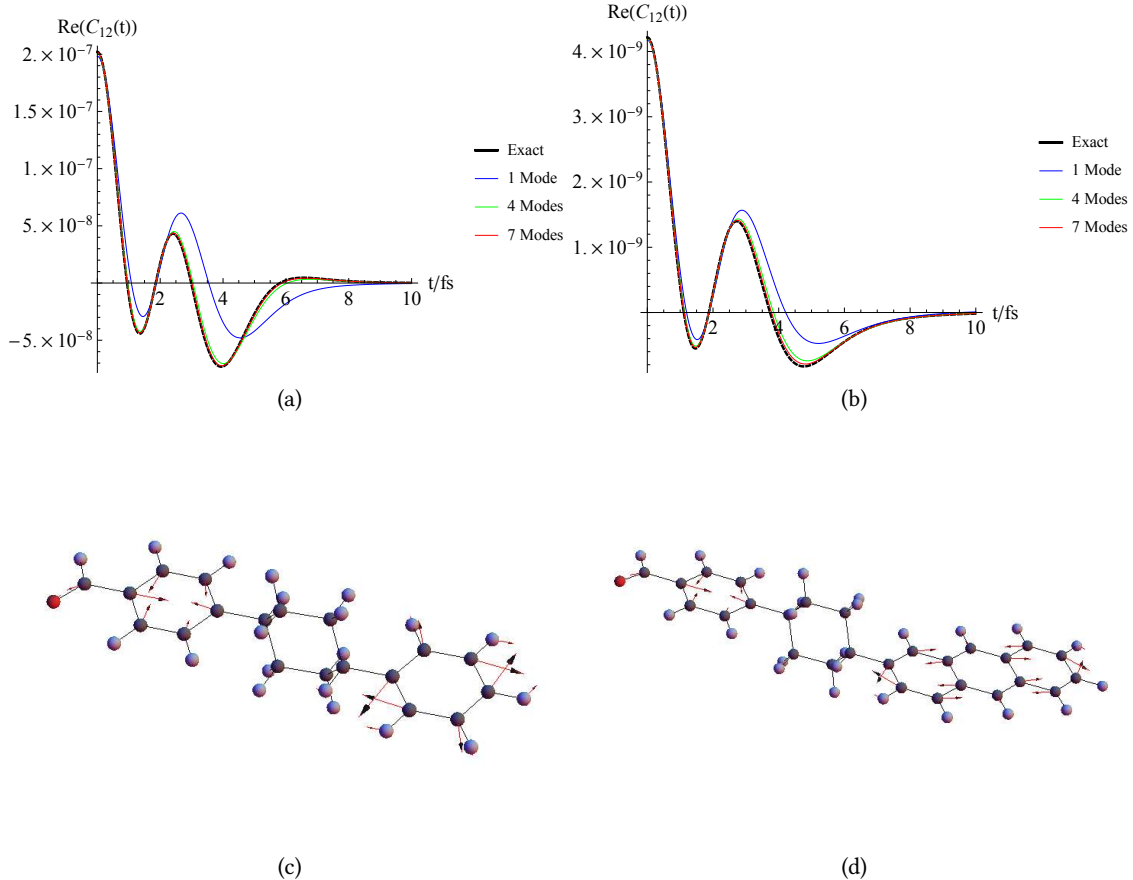
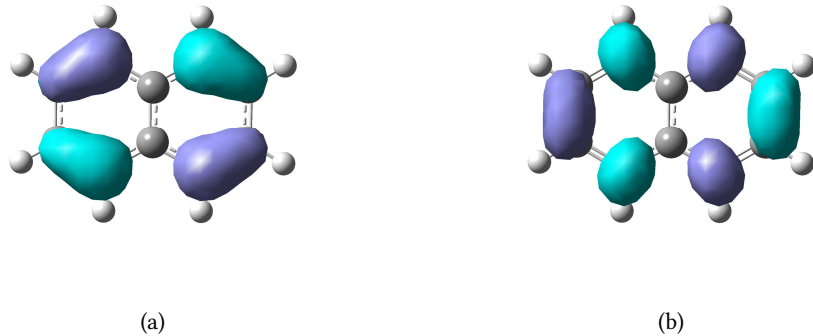


Figure 10: The correlation functions of projected modes for c14ee with the naphthalene moiety replaced by (a) phenyl ring and (b) anthracene, with their PLMs shown in (c) and (d).

modes or more, the excellent agreement with exact (all modes) result out to 10 fs indicates that the projection scheme provides an accurate description of the electronic coupling in these cases as well. Moreover, the PLMs are qualitatively similar to the PLM of unchanged c14ee. The displacements on the benzaldehyde moiety are almost identical, while on the phenyl and anthracene moieties they belong to totally symmetric irreducible representations as well.

It is not a coincidence that the PLMs belong to the totally symmetric irreducible representation of the isolated donor and acceptor moieties. This connection can be understood by analyzing the corresponding changes in the electron density that accompany the transition. For example, the

Figure 11: The (a) ( $A_u$ ) HOMO and (b) ( $B_{2g}$ )LUMO of naphthalene.

PLM on the naphthalene part shown in Fig. 8 largely corresponds to a symmetric ring-stretching mode, involving carbons C<sub>1</sub> - C<sub>2</sub>, C<sub>3</sub> - C<sub>4</sub>, C<sub>5</sub> - C<sub>6</sub>, and C<sub>7</sub> - C<sub>8</sub>. During the exciton transfer, an electron is promoted from the naphthalene HOMO to the naphthalene LUMO (shown in Fig. 11) and one expects that changes in the bond lengths should reflect the changes in electronic population. For naphthalene, a HOMO→LUMO transition would decrease the  $\pi$ -bond order between C<sub>1</sub> - C<sub>2</sub>, C<sub>3</sub> - C<sub>4</sub>, C<sub>5</sub> - C<sub>6</sub>, and C<sub>7</sub> - C<sub>8</sub>. Similar statements can be made for the phenyl and anthracene systems. In next section, we examine the PLMs and bond-length changes that occur during an energy transfer event. We show that, in a more quantitative way, while the PLMs can be understood in terms of geometric changes in the molecule, the reverse is not true. It is not at all straightforward to determine the PLMs by taking the difference between the initial and final geometries of the molecule.

## 2.4 LOCALIZED PROPERTY OF THE PRIMARY LANZCOS MODE

We have established that the Primary Lanzcos Mode is more like the normal modes of the isolated donor and acceptor moieties, rather than of the entire molecule. The relation between the PLM and

#### 2.4 LOCALIZED PROPERTY OF THE PRIMARY LANZCOS MODE

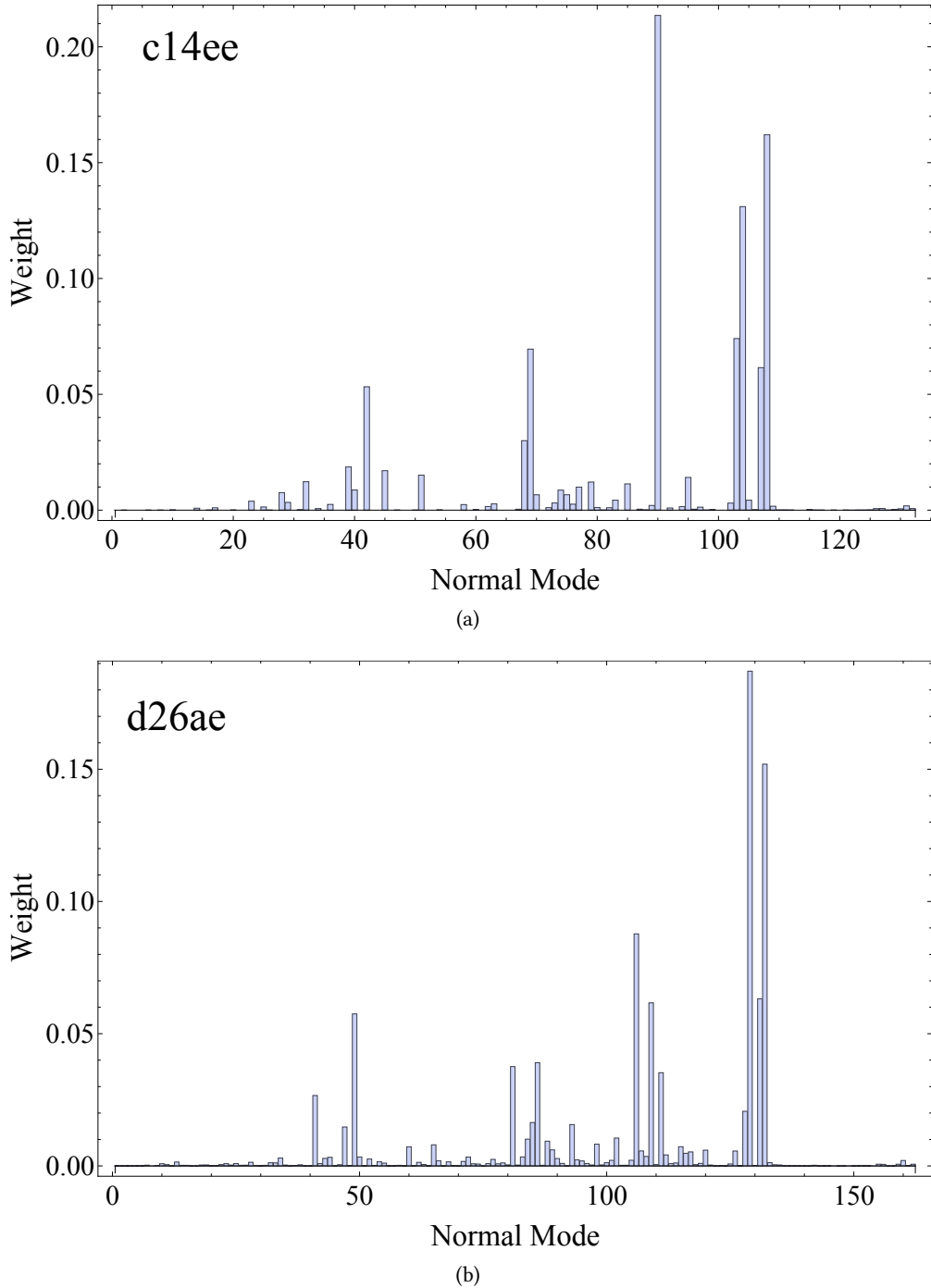


Figure 12: Projections of the PLM onto the normal modes of (a) c14ee and (b) d26ae.

#### 2.4 LOCALIZED PROPERTY OF THE PRIMARY LANZCOS MODE

bond length change partially verifies our statement. In this section, we explore the localization in greater detail. First, we project the PLM onto the normal modes of entire molecule, which is shown in Fig. 12, as a comparison to Fig. 9, where the normal modes of the individual moieties are used. It is clear that on the basis of entire molecule, more modes are significantly involved. This is in contrast to the projection of the PLM onto only the local modes of the isolated moieties, only a handful modes contribute. Since the PLM best captures the initial nuclear dynamics, its close relation with local sites reveals the fact that the exciton transfer here is more like a local excitation/de-excitation coupled by exchange interaction, in accordance with the Dexter mechanism [16].

One may argue that bridge is not included in our comparison. As showed in Fig. 8, one can see that very few motions involving the bridge contribute to the PLM. Thus, that we anticipate that we can construct the PLM using only local modes on the donor and acceptor units. In the next section, we quantitatively verify this by using only dominant modes on the donor and acceptor to construct coupling modes.

However, before we can compare different ways to construct the Lanczos modes, we first need to address a subtle problem. In the previous section, we symmetrized the geometry of naphthalene for the convenience in assigning irreducible representations to the vibrational modes. However, for constructing the modes for the entire unit one needs to use the optimized rather than symmetrized geometry. In Fig. 13 we show the project of the PLM onto the modes for optimized naphthalene. The irreducible representations have been roughly assigned to the dominant modes. The projections are almost same to the ones on the symmetrized geometry, except a new  $B_{2u}$  mode is involved in c14ee. However, it does not exist in d26ae. The reason is that the most significant mode of c14ee and d26ae are slightly different. The corresponding displacement vectors are embedded in Fig. 13. For c14ee, the dominant mode is not an exact  $A_g$  mode, because carbons move in the way of  $A_g$  while hydrogens behave like  $B_{2u}$ . On the contrary, d26ae has a mode more similar to  $A_g$ . As the result, in the projection of naphthalene in c14ee, a  $B_{2u}$  mode is needed to correct the hydrogen motions.

2.4 LOCALIZED PROPERTY OF THE PRIMARY LANZCOS MODE

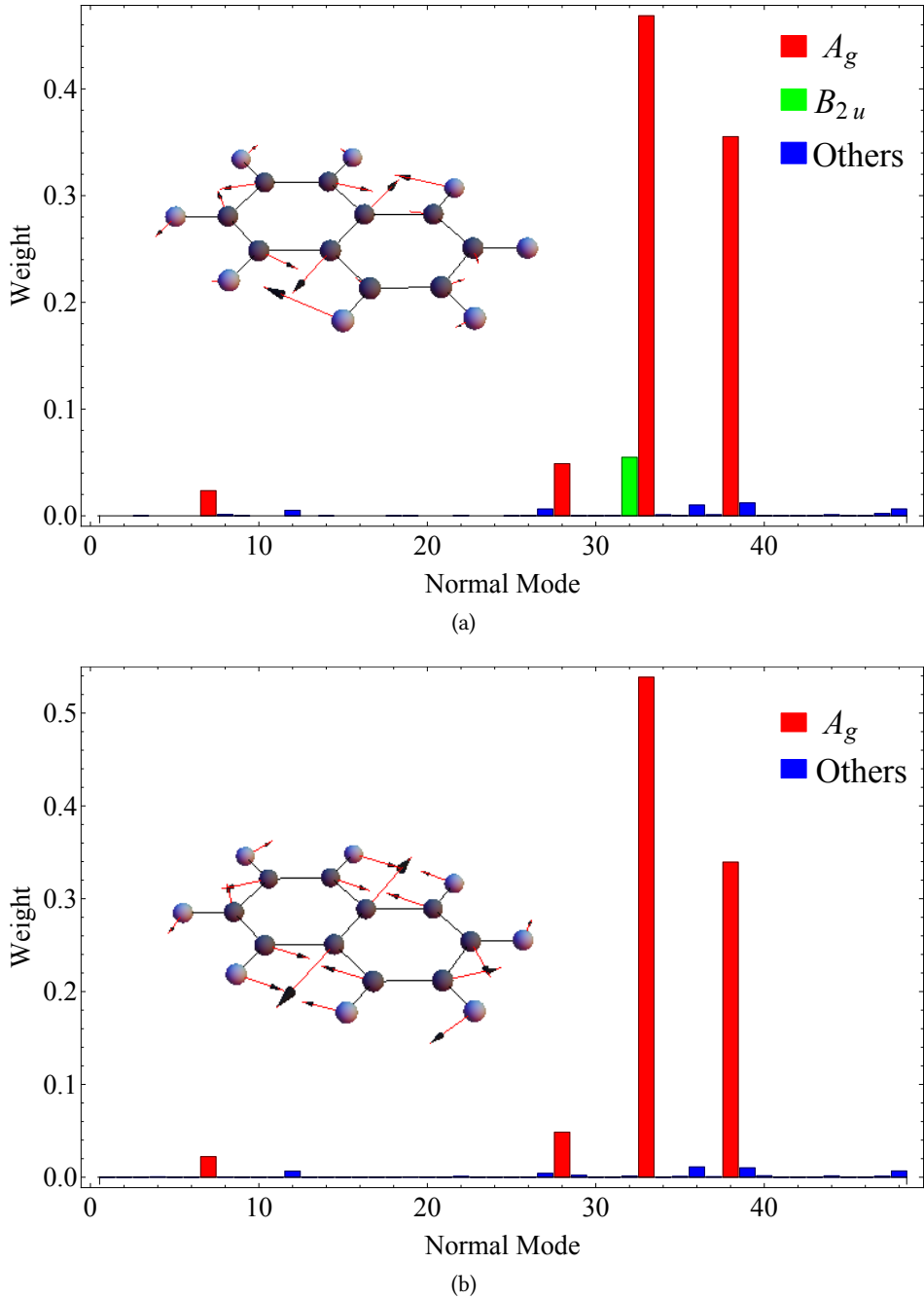


Figure 13: Projection of PLMs onto unsymmetrized naphthalene for (a) c14ee and (b) d26ae. They are almost same to Fig. 9(b) and (d) except for a mode with  $B_{2u}$  symmetry in c14ee. Embedded are the most significant modes, namely, the 33rd modes

To construct coupling modes, we collect a small number of modes on both naphthalene and benzaldehyde in the order of decreasing weights, then sum up the displacement vectors multiplied by their weights. We then bench-mark the quality of taking various different combinations of normal modes by computing the coupling auto-correlation function in Eq. 3 and comparing to the exact result obtained by including all modes. We denote these as  $NxBy$  where  $x$  denotes the number of naphthalene local modes and  $y$  denotes the number of benzaldehyde local modes used in each case.  $NfBf$  denotes that *all* local modes are included. The correlation functions and rate constants derived from various combinations of normal modes are summarized in Fig. 14.

First, if we take all local modes from both moieties, ( $NfBf$ ) the resulting approximated correlation function is indistinguishable from the exact correlation function. This verifies our observation that the bridge unit is not needed in constructing the PLM. In order to achieve adequate agreement with the exact correlation function, at least 10 of the strongest contributing local modes are needed from both the donor and acceptor units.

However, as seen on our previous work [12], the approximate correlation function does not need to give perfect agreement with the exact correlation function to produce an accurate transition rate constant (Eq. 4). To assess the accuracy of using different combinations of local modes, we calculate the transition rate constants for various combinations up to 10 modes on each moiety and compare to the exact rate. This data is summarized in the form of contour plots in Fig. 14(c,d). For the c14ee case, there is an optimal “valley” whereby taking 3 modes from benzaldehyde and 4-6 modes from naphthalene produces an agreement with the exact result to within 5%. For the d26ae case, fewer number of benzaldehyde modes than naphthalene modes are needed to give agreement to within 5% of the exact rate constant. This is easily anticipated since naphthalene is simply a larger molecule with more normal modes.

## 2.5 GEOMETRY CHANGE AND RELAXATION MODE

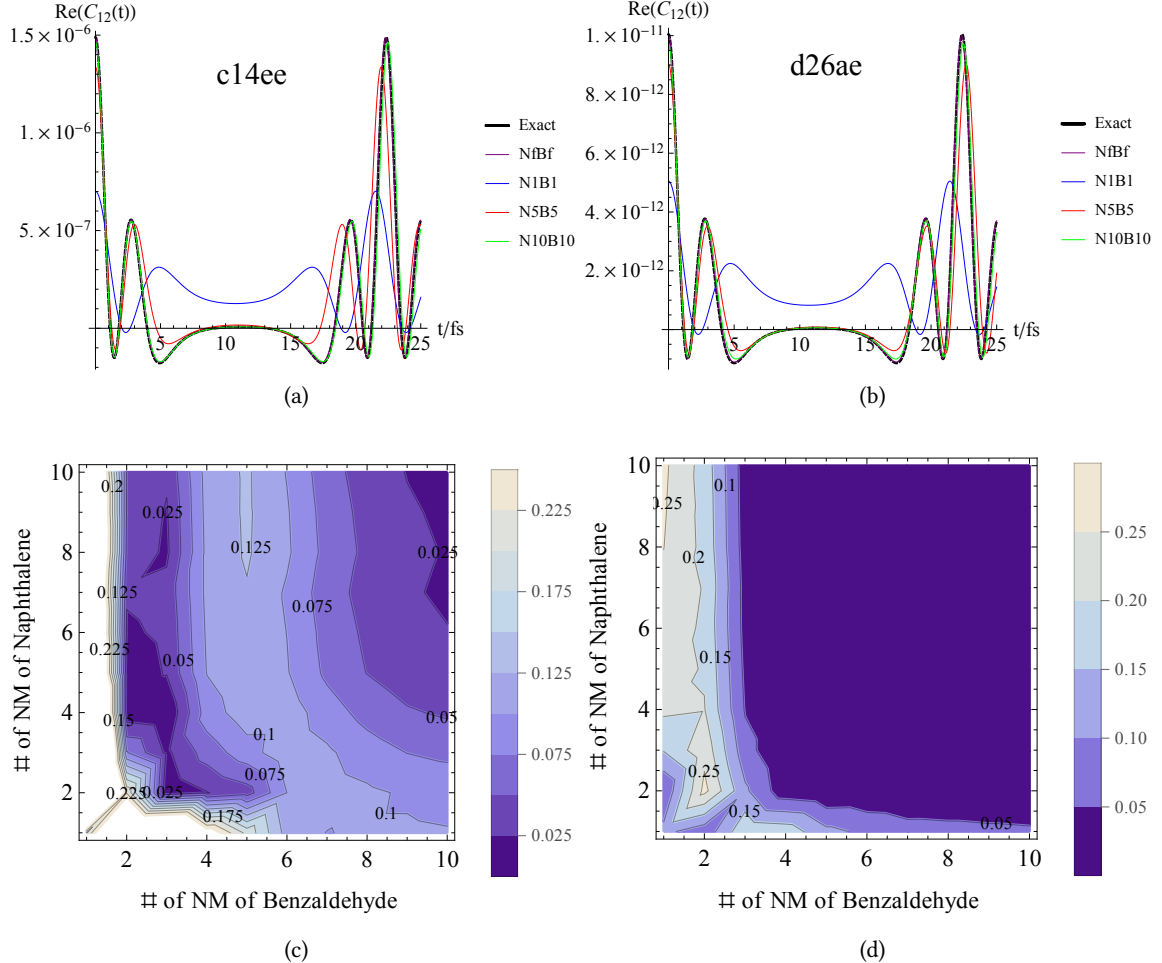


Figure 14: Correlation functions for different combinations of normal modes are shown for (a)  $c14ee$  and (b)  $d26ae$ . The “exact” ones refer are for the PLMs. “NfBf” is the mode made up from all normal modes of both the donor and acceptor sites. The designation “NxBy” indicates that the correlation function was constructed using  $x$  most significant normal modes on naphthalene and  $y$  most significant ones on benzaldehyde. Plots (c) and (d) show the relative error in rate constants calculated for various combinations of normal modes compared to the exact result or  $c14ee$  (c) and  $d26ae$  (d) respectively.

## 2.5 GEOMETRY CHANGE AND RELAXATION MODE

We showed that the PLMs agree with bond length changes on the moieties. We next consider the relation between the PLM and geometry change accompanying the transition. First, we use the

## 2.5 GEOMETRY CHANGE AND RELAXATION MODE

Table 3: Approximated geometry using the PLM and the relaxation modes (RM) compared to acceptor states

Mode used	C <sub>14ee</sub> -PLM	C <sub>14ee</sub> -DNM	D <sub>26ae</sub> -PLM	D <sub>26ae</sub> -DNM
Max. bond length difference (Å)	0.034	0.160	0.039	0.283
Max. bond angle difference (rad)	0.053	0.075	0.057	0.135

PLM to approximate geometry change by distorting the molecule along the PLM. The magnitude of the distortion is determined by minimizing the average bond length difference of the four bonds on naphthalene which stretch significantly in PLM, between the optimized and approximate geometries. In Table 1 we list the differences between two geometries. Comparing the maximum difference of bond lengths and angles between the approximated and true final states (Table. 3), the differences are very small, so PLMs seem to give fairly good approximations of geometry changes.

However, this is only one side of the story and we need try to do this in reverse, *i.e.*, can we determine the PLM from simply geometric changes accompanying the transition? To see if this is possible, we can project the geometry change onto the normal modes of molecule and moieties respectively. The results for our two test cases are shown in Fig. 15 and 16.

When projected onto the whole molecule, we see that geometry change is mostly dominated by one very low frequency mode corresponding to an internal torsion of the entire donor-bridge-acceptor molecule. Compared to the PLMs in the same basis in Fig. 12 we see that PLMs have many more modes involved. However, if we compare the projections onto the moieties in Fig. 9 and 15, the geometry changes resemble PLMs well, except in the low frequency region. In essence, simply changing representation completely changes the implied dynamics.

The resolution to this inconsistency is to distinguish between the two types of geometric changes. One is the internal changes within the moieties. These are well represented by the PLM. The other is the gross motion of the entire molecule, which we shall refer to as the “relaxation mode” (RM). This latter motion is not well represented by the PLM. These two kinds of motion correspond to two different steps that accompany the electronic transition. The internal motion primarily affects C=C bond lengths, and hence is strongly coupled to the  $\pi$ -electronic degrees of freedom, while gross

## 2.5 GEOMETRY CHANGE AND RELAXATION MODE

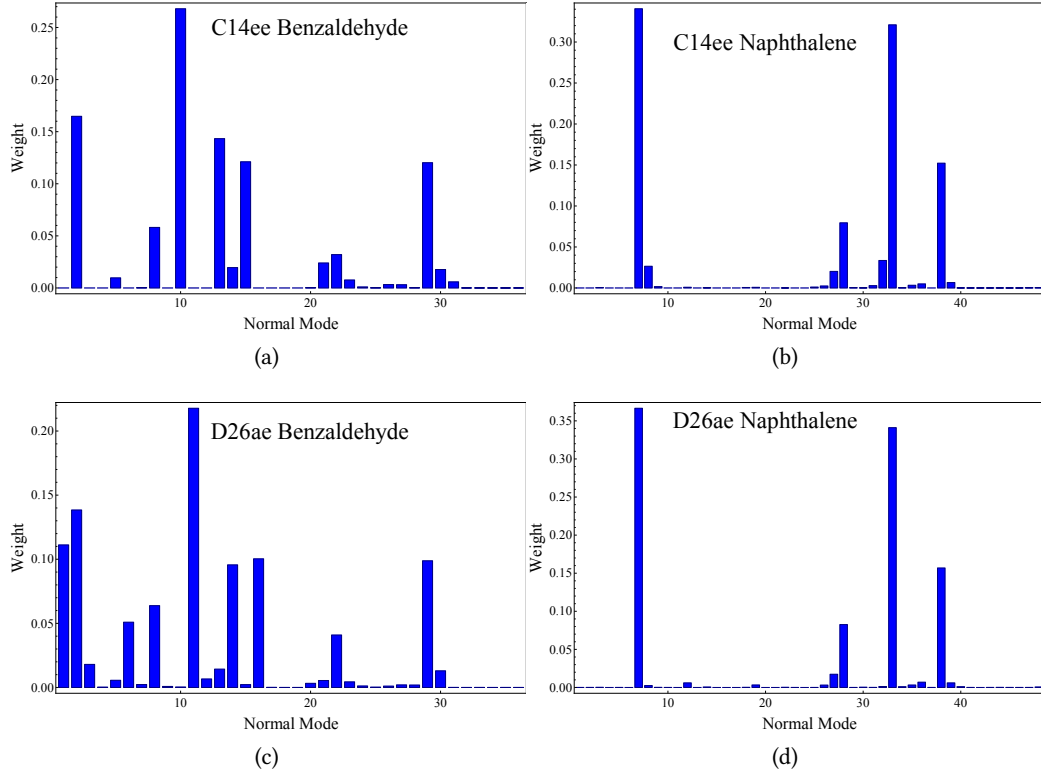


Figure 15: Projections of the geometry change between initial and final states onto the normal modes of (a) benzaldehyde and (b) naphthalene sites in c14ee, and d26ae in (c) and (d). Except for some low frequency modes, they are similar to the projections of PLM.

motion of moieties corresponds to relaxation after exciton transfer has occurred. This is verified in Table 1, where we use the relaxation mode to approximate the final geometry. The procedure is similar to that of PLM. Although RM is the dominant mode in the projection, it gives much worse approximated bond lengths and angles.

Since the PLM explains the short-time dynamics and can approximate the local geometry changes within the individual moieties very well, we anticipate that the PLMs facilitate the energy transfer step. To verify our prediction, we computed correlation functions of the electron/phonon coupling operators (Eq. 4) using different subsets of nuclear motions to estimate the couplings: PLM, RM, geometry change (GC), and geometry change with the RM component eliminated (GC-RM). The

## 2.5 GEOMETRY CHANGE AND RELAXATION MODE

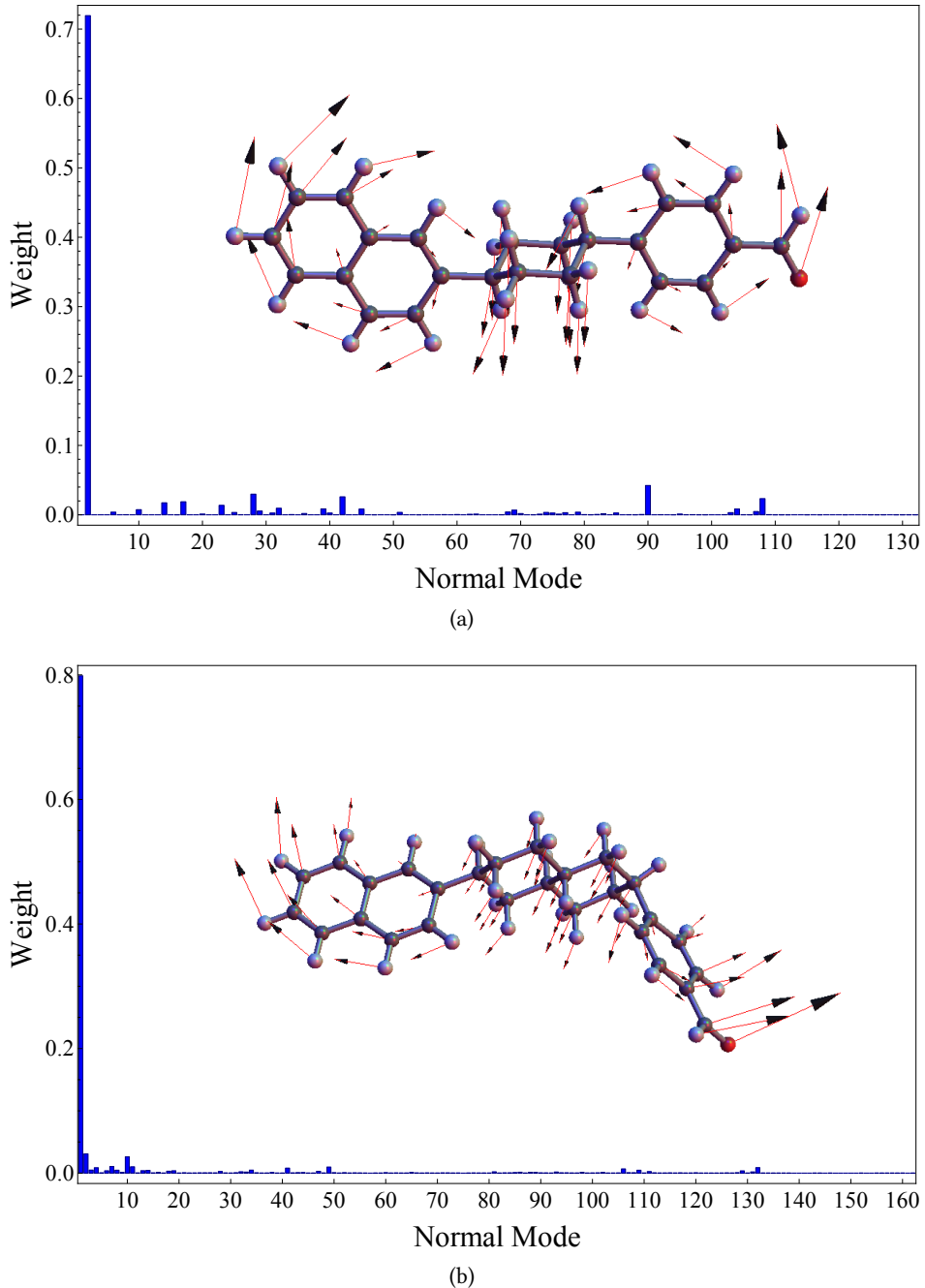


Figure 16: Projections of the geometry change between initial and final states onto the normal modes of (a) c14ee and (b) d26ae. They are both dominated by single mode, the relaxation mode (RM), which is embedded.

## 2.6 DISCUSSION

latter two correspond to taking the total geometric difference between the initial and final states of the molecule and projecting this onto normal modes, and to taking the geometric difference and subtracting off the relaxation mode. The various correlation functions and rate constants are summarized in Fig. 17. The exact results are obtained by using all normal modes and couplings. The PLM gives nearly perfect agreement to the exact calculation for both the time-correlation functions (Fig. 17) and the computed rates for both molecules considered (Fig. 18). The relaxation mode (RM) gives no contribution to the correlation function or the rate. Finally, using just the over-all geometric change (GC) gives a poor estimate of both the correlation function and the rate. GC-RM gives the initial transient dynamics in the correlation function and a reasonable approximation to the overall rate. However, the best agreement overall is obtained by using the PLM identified using the Lanczos search algorithm.

## 2.6 DISCUSSION

We presented here a further exploration of the classes of nuclear motions that accompany an electronic energy transition. We show that deeper insight can be gained by analyzing the primary modes and comparing them to both the geometric distortion of the molecule and to the electronic orbitals involved in the transition.

Our results also suggest that the energy transfer process in these systems occurs in two distinct steps. The initial transfer from the donor to acceptor occurs in a fixed nuclear frame—as per the Condon principle. This fast transfer is facilitated by the PLM and involves excitations in the C=C bond lengths of donor and acceptor fragments in accordance with changes in the HOMO/LUMO populations of each fragment. After the exciton transfer, the entire molecule undergoes a slow but large geometric relaxation under the new electronic distribution.

Finally, we emphasize that the PLM approach and this analysis need not be limited to the energy transfer cases studied here. Combined with the time-convolutionless master equation approach,

## 2.6 DISCUSSION

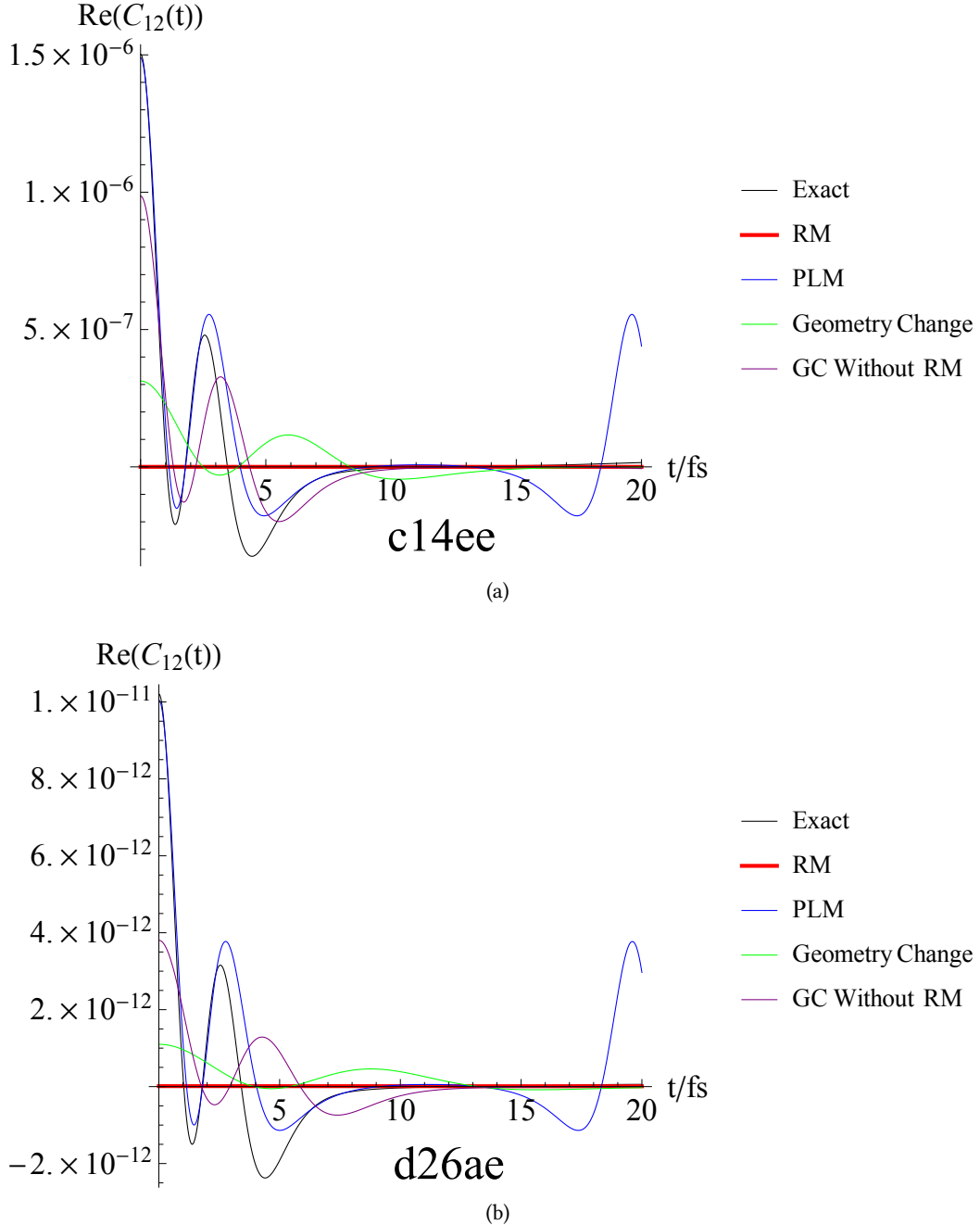


Figure 17: Correlation functions of relaxation mode (RM), PLM, geometry change (GC), and geometry change with the RM component eliminated for (a) c14ee and (b) d26ae. The exact rate is computed using the full set of normal modes.

## 2.6 DISCUSSION

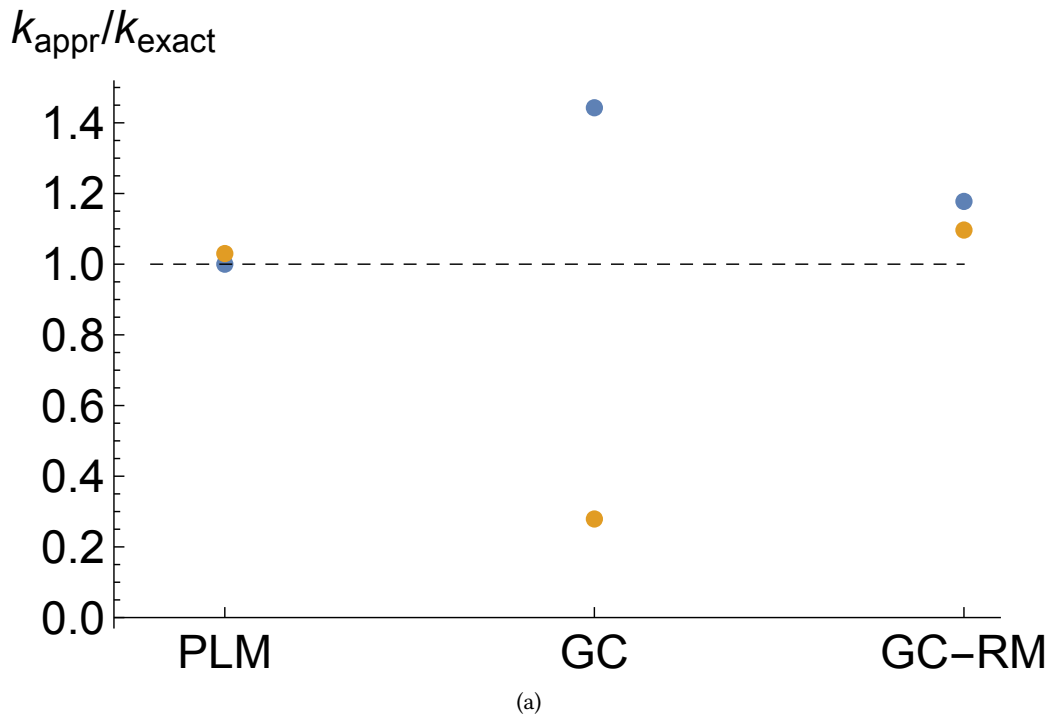


Figure 18: Relative comparison of the rate constants computed using different sets of reduced modes. blue = c14ee, gold =d26ae.

this provides a robust and efficient way for computing state-to-state transitions rates for a wide class of molecular systems.

## BIBLIOGRAPHY

---

- [1] R. A. Marcus, *The Journal of Chemical Physics* **24**, 966 (1956).
- [2] R. A. Marcus, *The Journal of Chemical Physics* **43**, 679 (1965).
- [3] R. A. Marcus, *Reviews of Modern Physics* **65**, 599 (1993).
- [4] J. Miller, L. Calcaterra, and G. Closs, *Journal of the American Chemical Society* **106**, 3047 (1984).
- [5] G. L. Closs, P. Piotrowiak, J. M. MacInnis, and G. R. Fleming, *Journal of the American Chemical Society* **110**, 2652 (1988).
- [6] G. L. Closs, M. D. Johnson, J. R. Miller, and P. Piotrowiak, *Journal of the American Chemical Society* **111**, 3751 (1989).
- [7] A. Pereverzev and E. R. Bittner, *The Journal of Chemical Physics* **125**, 104906 (2006).
- [8] H. Tamura, J. G. S. Ramon, E. R. Bittner, and I. Burghardt, *Physical Review Letters* **100**, 107402 (2008).
- [9] H. Tamura, E. R. Bittner, and I. Burghardt, *The Journal of Chemical Physics* **126**, 021103 (2007).
- [10] J. Singh, E. R. Bittner, D. Beljonne, and G. D. Scholes, *The Journal of Chemical Physics* **131**, 194905 (2009).
- [11] E. R. Bittner and C. Silva, *Nat Commun* **5**, 3119 (2014).
- [12] X. Yang and E. R. Bittner, *The Journal of Physical Chemistry A* **118**, 5196 (2014).

## Bibliography

- [13] J. E. Subotnik, J. Vura-Weis, A. J. Sodt, and M. A. Ratner, *The Journal of Physical Chemistry A* **114**, 8665 (2010).
- [14] M. K. Grover and R. Silbey, *The Journal of Chemical Physics* **52**, 2099 (1970).
- [15] M. Rice and Y. N. Gartstein, *Physical review letters* **73**, 2504 (1994).
- [16] D. L. Dexter, *The Journal of Chemical Physics* **21**, 836 (1953).